Title
Visualizing Transcranial Direct Current Stimulation (tDCS) in vivo using Magnetic Resonance Imaging

Author
Jog, Mayank Anant

Publication Date
2017

Peer reviewed|Thesis/dissertation

UNIVERSITY OF CALIFORNIA

Los Angeles

Visualizing Transcranial Direct Current Stimulation (tDCS) *in vivo* using Magnetic Resonance Imaging

A dissertation submitted in partial satisfaction of the
requirements for the degree Doctor of Philosophy
in Biomedical Engineering

by

Mayank Anant Jog

2017

ABSTRACT OF THE DISSERTATION

Visualizing Transcranial Direct Current Stimulation (tDCS) *in vivo* using Magnetic Resonance Imaging

by

Mayank Anant Jog
Doctor of Philosophy (Candidate) in Biomedical Engineering
University of California, Los Angeles 2017
Professor Danny Jiong Jiong Wang, Co-Chair
Professor Mark S. Cohen, Co-Chair

Transcranial Direct Current Stimulation (tDCS) is a low-cost, non-invasive neuromodulation technique that has been shown to treat clinical symptoms as well as improve cognition. However, no techniques exist at the time of research to visualize tDCS currents *in vivo*. This dissertation presents the theoretical framework and experimental implementations of a novel MRI technique that enables non-invasive visualization of the tDCS electric current using magnetic field mapping. The first chapter establishes the feasibility of measuring magnetic fields induced by tDCS currents. The following chapter discusses the state of the art implementation that can measure magnetic field changes in individual subjects undergoing concurrent tDCS/MRI. The final chapter discusses how the developed technique was integrated with BOLD fMRI–an established MRI technique for measuring brain function. By enabling a concurrent measurement of the tDCS current induced magnetic field as well as the brain's hemodynamic response to tDCS, our technique opens a new avenue to investigate tDCS mechanisms and improve targeting.

The dissertation of Mayank Anant Jog is approved.

Daniel Ennis

Peng Hu

Marco Iacoboni

Danny Jiong Jiong Wang, Committee Co-Chair

Mark S. Cohen, Committee Co-Chair

University of California, Los Angeles

2017

DEDICATION

I would like to dedicate this dissertation…

First and foremost, to the people who made this work possible: My professors, the people at LOFT lab, the brain mapping center and UCLA. To my parents, grandparents and the many, many people who have been integral in my development as a person. I would not be here, doing what I do, without your example.

To the endeavor of developing affordable healthcare solutions. It is rare indeed, to work on a technology that is simple, easy-to-use, affordable, portable and potentially has wide clinical application. I sincerely hope that my contribution (through this dissertation, and subsequent work) can help improve our understanding of tDCS, and ultimately help translate it into an effective and affordable healthcare option.

Chapters

ACKNOWLEDGEMENTS

Chapter 1 is based on the work: Jog, M. et al. In-vivo Imaging of Magnetic Fields Induced by Transcranial Direct Current Stimulation (tDCS) in Human Brain using MRI. *Scientific Reports*, 6, 34385; doi: 10.1038/srep34385 (2016). M.J., R.X.S., K.J. and D.J.J.W. designed and performed the experiments. M.J., R.X.S., K.J., W.D. and D.J.J.W. analyzed data. M.J., W.D., A.W. and D.J.J.W. wrote the manuscript. B.L., D.T., L.P. and M.B. contributed simulation tools.

Chapter 2 is based on (a) the work: Jog, M. et al. Evaluation of a novel MRI technique for mapping in-vivo currents and hemodynamic changes during tDCS. Proceedings #16, *Brain Stimulation: Basic, Translational, and Clinical Research in Neuromodulation*, Volume 10, Issue 4, e64 - e66 (2017), and (b) work in preparation for publication: Jog, M., Yan, L., Jann, K. and Wang, D.J.J. A novel dual-echo EPI implementation for *in-vivo* current mapping in individual subjects during transcranial Direct Current Stimulation (tDCS). M.J. and D.J.J.W. wrote the manuscript, L.Y. developed the data acquisition technique, and K.J. contributed in data analysis.

Chapter 3 is based on the work: Jog, M. et al. Evaluation of a novel MRI technique for mapping in-vivo currents and hemodynamic changes during tDCS. Proceedings #16, *Brain Stimulation: Basic, Translational, and Clinical Research in Neuromodulation*, Volume 10, Issue 4, e64 - e66 (2017). M.J. and D.J.J.W. wrote the manuscript, L.Y. developed the data acquisition technique, and K.J. contributed in data analysis.

Mayank Anant Jog

PhD Candidate
Brain Mapping Center, 660 Charles E Young Drive South, Los Angeles, CA 900695
Email: *mayankjog@gmail.com*

EDUCATION

UCLA (University of California Los Angeles), ***Aug 2011-Current***

- → PhD Biomedical Engineering Inter-Departmental Program (BME IDP)
  Advanced to doctoral candidacy, ***13th Sept 2013***
- → Masters Biomedical Engineering Inter-Departmental Program (BME-IDP)
  Awarded December 2016

BITS (Birla Institute of Technology and Science) **Pilani, Goa Campus,** ***July 2006-June 2011***

- → B.E. (Hons.) Electrical and Electronics Engineering
- → B.E. (Hons.) Computer Science

PUBLISHED RESEARCH

Jog, M., Yan, L., Jann. K., Wang, D.J. Evaluation of a novel MRI technique for mapping in-vivo currents and hemodynamic changes during tDCS. Proceedings #16, *Brain Stimulation: Basic, Translational, and Clinical Research in Neuromodulation*, Volume 10, Issue 4, e64 - e66 (2017)

Jog, M., Smith, R.X., Jann, K., Dunn, W., Lafon, B., Truong, D., Wu, A., Parra, L., Bikson, M., Wang, D.J. In-vivo Imaging of Magnetic Fields Induced by Transcranial Direct Current Stimulation (tDCS) in Human Brain using MRI. *Scientific Reports*. Oct 4;6:34385 (2016)

Jog, M., Yan, L., Kilroy, E., Krasileva, K., Jann, K., LeClair, H., Elashoff, D., Wang, D.J. Developmental trajectories of cerebral blood flow and oxidative metabolism at baseline and during working memory tasks. *Neuroimage*. Jul 1;134:587-96 (2016)

Yan, L., Liu, C.Y., Smith, R.X., Jog, M., Langham, M., Krasileva, K., Chen, Y., Ringman, J.M., Wang, D.J. Assessing intracranial vascular compliance using dynamic arterial spin labeling. *Neuroimage*. Jan 1;124 (Pt A):433-41 (2016)

Cha, Y.H., Jog, M., Kim, Y.C., Chakrapani, S., Kraman, S.M., Wang, D.J. Regional correlation between resting state FDG PET and pCASL perfusion MRI. *Journal of Cerebral Blood Flow & Metabolism*. Dec;33(12):1909-14 (2013)

CONFERENCE TALKS

Jog, M.**,** Yan, L., Jann, K. & Wang, D.J. (2017). Evaluation of a novel MRI technique for mapping in-vivo currents and hemodynamic changes using tDCS. Oral presentation at the annual Brain Stimulation and Imaging Meeting, Vancouver

Jog, M., Smith, R., Jann, K., Dunn, W., Wu, A. & Wang, D.J. (2015). In-vivo MRI mapping of electrical current of transcranial Direct Current Stimulation. Oral presentation at the annual International Conference of the Organization for Human Brain Mapping (OHBM), Hawaii.

Jog, M., Smith, R., Jann, K., Dunn, W., Wu, A. & Wang, D.J. (2015). In-vivo Evidence of transcranial Direct Current Stimulation (tDCS) induced magnetic-field changes in Human Brain revealed by MRI. Oral presentation at the annual Brain Stimulation and Imaging Meeting, Hawaii.

FELLOWSHIPS & AWARDS

1. Merit Award, International Conference of the Organization for Human Brain Mapping (2017)
2. Dissertation Year Fellowship, UCLA (2016)
3. Merit Award, International Conference of the Organization for Human Brain Mapping (2015)
4. Educational Stipend, Conference of the International Society for Magnetic Resonance in Medicine (2015)
5. Educational Stipend, Conference of the International Society for Magnetic Resonance in Medicine (2014)
6. Neuro-Imaging Training Program Predoctoral Fellowship, UCLA (2013-2014)
7. Educational Stipend, Conference of the International Society for Magnetic Resonance in Medicine (2013)
8. Graduate Division Fellowship, UCLA (2011)
9. Merit Scholarship, BITS-Goa, India (2009-2011)
10. Merit Scholarship, BITS-Goa, India (2006-2008)

CREATIVE CONTRIBUTIONS

- ✓ Finalist in the "UCLA GradSLAM: Storytelling your research in 3 minutes" competition (2016) (https://www.youtube.com/watch?v=Fm8kJ2xZ-1I)

Introduction

1. Brief overview of tDCS

1.1 Background

Transcranial Direct Current Stimulation (tDCS) is part of an emerging array of non-invasive and non-pharmacological neuromodulation techniques that uses milliampere electric currents applied at the scalp. As shown in Fig. 1, a typical tDCS setup involves a 2-electrode montage applied on the surface of the head to deliver constant current.

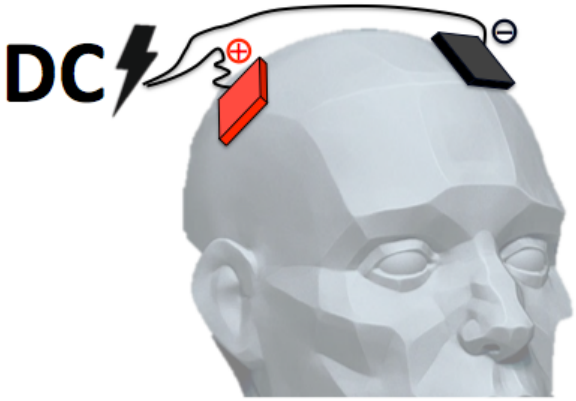

Figure 1. Typical tDCS setup: A typical tDCS montage consists of two electrodes (Anode and Cathode) placed on the scalp to deliver mA direct current. Conductivity gel is used between electrodes and the scalp to ensure good electrical contact.

In contrast to other neuromodulation techniques such as Transcranial Magnetic Stimulation (TMS) and Electroconvulsive Therapy (ECT), tDCS is incapable of directly inducing action potentials, and as a result can be considered a neuromodulatory intervention(1).

As shown in Fig. 2 ((a)–(e)), the physical parameters in a typical tDCS experiment are:

(a) Current intensity and duration:

tDCS has been reported to change cortical excitability (2, 3). The efficacy of tDCS in inducing these changes depends on the applied current intensity. Larger current intensities and/or longer durations result in stronger effects of tDCS(4-6). At present, safety concerns limit the maximum current intensity and duration that can be used. Typically, the tDCS dose is kept at or below 2mA for generally 10-15min(7).

(b) Electrode montage:

tDCS is hypothesized to enhance/suppress cortical excitability depending on the polarity of the stimulating electrode. By convention, the positively charged electrode is called the anode while the negatively charged electrode is the cathode. The anode(/cathode) is found to increase(/decrease) excitability of superficial cortical neurons (1). Extending the anode-cathode idea, tDCS montages have evolved to using multiple electrodes ("high definition tDCS") that show better efficacies (8, 9).

(c) Electrode placement:

A typical tDCS setup can have one electrode over the target area, and the reference electrode over a control area (unilateral tDCS). For instance, in an application targeting the primary motor cortex (M1), a unilateral placement would consist of placing the anode over the target M1 and cathode over the contralateral supraorbital area. In contrast, a bilateral placement would have the cathode electrode over the contralateral M1 area. The pros and cons of unilateral vs. bilateral montages are still being investigated (10, 11).

(d) Cognitive paradigms (tasks/rest):

A tDCS experiment typically includes a cognitive paradigm to evaluate the effects of tDCS. For example: A Purdue Pegboard task can be used for studies involving motor function (12). The Purdue pegboard task is a timed test used to measure manual dexterity and brain function. Participants are asked to place pins into matching holes in the pegboard using a specific hand. Another example is assigning magnitudes to symbols, and using a numerical stroop task for studies involving learning (13).

(e) Participant population:

The participants in a tDCS study can be drawn from a pool of healthy volunteers, a clinical population or a combination of the two (case-control studies) (14-19). Effects of tDCS have also been investigated in pediatric populations (20-22). A 2016 review by Bikson et al. (23) notes that the no adverse effects or irreversible injuries have been reported from the use of conventional tDCS in human trials. While a mild tingling/itching sensation under the electrodes can be perceived during tDCS, these effects are transient and fade over time. The low-cost, simple setup, portability and tolerability of tDCS make it particularly well suited for research across different populations (compared to other neuromodulatory interventions e.g. TMS).

The full range of tDCS parameters explored in on-going research are shown in Fig. 2. (White Pane (a)–(e)). Imaging techniques add a new dimension to tDCS research by enabling measurements of the brain's response to tDCS *in vivo* (Fig. 2. (I), Blue Pane). Among the set of available imaging techniques (including EEG, MEG, FDG-PET) functional MRI has been a popular choice to study tDCS, because it provides uniform millimeter spatial resolution, and

temporal resolution on the order of seconds. The goal of my research was to develop a technique to visualize the tDCS currents *in vivo* (as shown in Fig. 2. (I^P), Yellow Pane), and thus complement existing imaging techniques that measure the response of the brain to tDCS. At the time of research, no techniques exist to visualize tDCS currents, and tDCS targeting was performed using computational models (which also need *in vivo* validation).

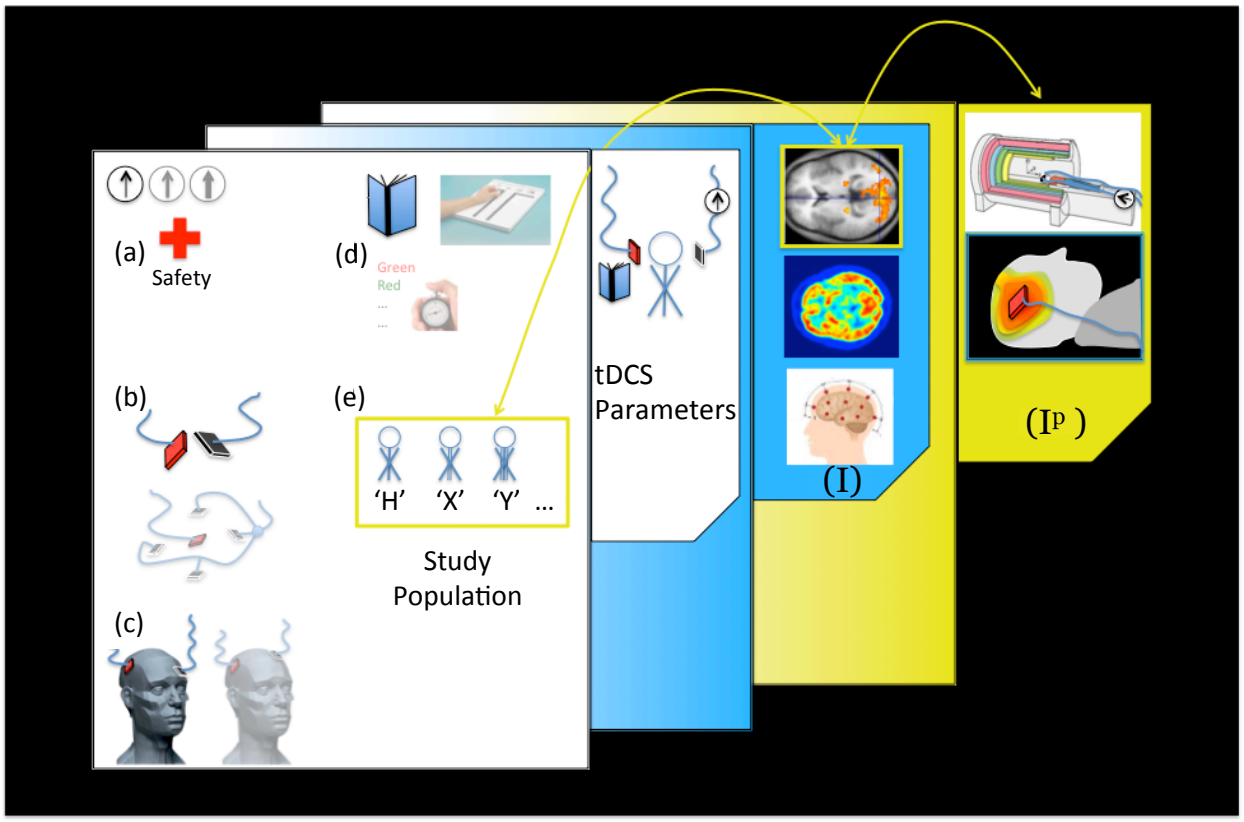

Figure 2. Research in tDCS: WHITE pane shows the parameters in a typical tDCS investigation: (a) Current intensity and duration (limited by safety), (b) electrode arrangements, (c) electrode placement, (d) cognitive paradigms (task/rest), and (e) population. BLUE pane shows imaging techniques used in tDCS research (MRI, PET and EEG are shown). YELLOW pane (I^p) depicts the proposed imaging technique in context: The capability to visualize tDCS currents *in vivo* is expected to complement existing imaging techniques that measure the response of the brain to tDCS.

1.2 Clinical significance

Since the demonstration of tDCS induced sustained changes in motor evoked potentials (MEP)(2, 3) research in tDCS has grown exponentially, as shown in Fig. 3. tDCS has been shown to improve symptoms in a wide range of neurologic and psychiatric disorders (including epilepsy, Parkinson's disease, chronic pain, depression, drug cravings, and stroke(7, 18, 24-39)). tDCS has also been shown to enhance learning, modulate working memory, and impart other cognitive benefits in healthy subjects(14, 17, 40, 41). Given its simple setup, high safety and low cost(23, 41), tDCS is emerging as a potential therapy as well as a tool for understanding the neurophysiology underlying various cognitive functions.

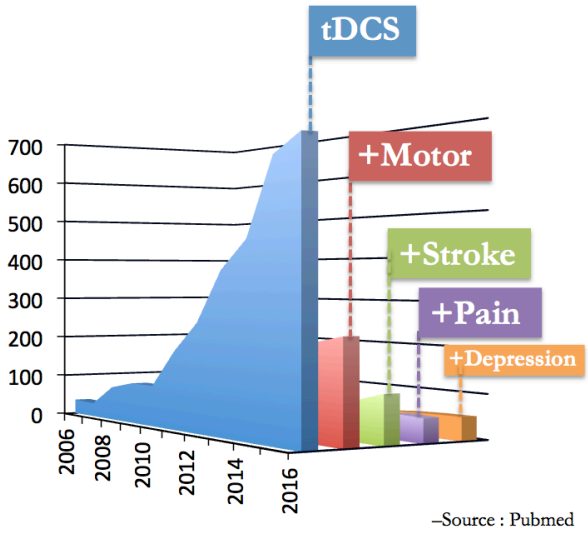

Figure 3. Publications in the field of tDCS since 2006: Since the seminal paper by Nitsche and Paulus (2, 3) reporting tDCS induced cortical excitability changes, research in tDCS has grown exponentially over the years. This research has included neurophysiology investigations (for instance, analyzing tDCS induced excitability changes in the motor cortex) as well as translational investigations exploring treatment of symptoms in stroke, pain and depression (shown by '+…' in figure).

1.3 Safety

An earlier safety study by Poreisz C. et al. (41) using a montage of two electrodes (35 cm^2 area) over 77 normal subjects revealed no adverse side effects of tDCS. The study included 6 post-stroke, 9 migraine and 10 tinnitus patients who also did not experience any adverse side

effects. A recent safety review confirms this observation: as reported in Bikson et. al (23), conventional tDCS protocols in human trials (≤ 40 min, ≤ 4 mA, ≤ 7.2 Coulombs) have not produced any serious adverse effects or irreversible injuries over 33,200 sessions and 1000 subjects with repeated sessions.

2. Computational Modeling in tDCS research

The earliest computational models of the tDCS(42, 43) were built for a spherical head model. Since then, more sophisticated models have been developed that take into account head anatomy(44) of individual subjects. As described in Truong et al. (45), these models work by (i) segmenting human head data into different tissues, (ii) 3D modeling of the electrode montage, (iii) generation of finite element meshes (to solve the PDE of (v)), (iv) assigning resistivity values to each tissue, and (v) solving Laplace's equation over the finite element mesh. This approach has been applied to derive the optimal electrode montage and dosage for tDCS(46, 47), as well as the design of ring electrodes with focal distribution of tDCS current(48).

3. MRI in tDCS research

The applied tDCS current is hypothesized to enhance or suppress cortical excitability under the Anode or Cathode respectively. However, the precise mechanism of action of tDCS is still unknown(49). In order to understand the mechanisms of tDCS, there is a critical need to identify, given a particular tDCS montage, (a) the brain areas that the applied current passes through, and (b) the neural circuits that it modulates (which may extend beyond the site of stimulation through brain networks).

Magnetic Resonance Imaging (MRI) is an imaging technology that utilizes non-ionizing radiofrequency (RF) pulses to generate contrasts. The Blood Oxygenation Level Dependent (BOLD) contrast in MRI is generated by fluctuations in the deoxyhemoglobin concentration. Deoxyhemoglobin is paramagnetic, and a higher concentration of deoxyhemoglobin results in a reduction of the local MRI signal. Discovered in 1990 by Seiji Ogawa (AT&T Bell labs), the BOLD signal can be used to map neuronal activity changes in the brain(50-52). At the physiological level, an increase in regional neuronal activity increases the local demand for oxygen. The cerebral vasculature responds by increasing the blood flow to the area and overcompensating the demand, thereby making the area appear bright on the MRI scan.

A limitation of the BOLD signal is that it is essentially a qualitative metric, and is not linked to a physiologically quantitative value. Arterial Spin Labeling (ASL) addresses this need by using magnetically labeled arterial blood water as an endogenous tracer to measure Cerebral Blood Flow (CBF) and Perfusion(50, 53). The measured CBF changes act as a surrogate marker

for neuronal activity changes (based on neurovascular coupling), with the added advantage that the CBF values represent an actual physiological quantity(53).

Both BOLD and ASL are surrogate markers of changes in neuronal activity, and together constitute functional MRI (fMRI) - a category of MRI tools used to study brain function. To date, results from BOLD fMRI indicate that tDCS elicits long-lasting, polarity dependent changes in BOLD signal and network connectivity during motor, visual and language tasks(54-58). BOLD fMRI has also been used to guide tDCS electrode placement, as reported by Clark et al(59). In this study, rate of learning in a cognitive task was improved by tDCS modulation of regions identified using BOLD fMRI. Polarity dependent changes in regional cerebral blood flow measured using ASL fMRI have also been reported, both during and following tDCS stimulation(60). Overall, because fMRI uses non-ionizing RF to non-invasively image brain function at a millimeter-second spatio-temporal resolution, it is an ideal technique to investigate the neural circuits modulated by tDCS *in vivo*.

In parallel to identifying neural circuits modulated by tDCS, computational modeling has been used to predict brain regions the tDCS current passes through or directly engages, as described in the previous section. However, the distribution of tDCS current is influenced by a host of interacting factors not fully accounted for by computational models. These include electrode geometry, electrical properties of tissue and cerebrospinal fluid (CSF), CSF flow, and complicated boundary conditions (due to the convoluted brain surface morphology). To date, estimates of the tDCS current distribution remain theoretical and await experimental validation.

The idea of visualizing electric currents through measurements of magnetic fields was first proposed by Joy et al (61). In this work, electric current was synchronized with RF pulses of MRI pulse sequence, and magnetic fields induced by switching electric currents in a phantom as well as human forearm were measured using MRI. Since then, the current mapping research has diverged into (62):

(a) Low Frequency Current Density Imaging (LF-CDI): This builds on the original approach of Joy et al (61) in imaging magnetic fields induced by externally applied switching currents.

(b) Radio-Frequency Current Density Imaging (RF-CDI): This uses the Bloch-Siegert Shift (63-65), an effect that becomes observable at magnetic field fluctuations induced by electric currents switching near the MRI center frequency (~64 and 128 MHz for 1.5 and 3T respectively).

(c) A third technique to visualize electric currents supplements (a) with voltage measurements made on the surface of the conductor volume (MREIT (66-68)). This technique was developed to calculate conductivities of the underlying tissue, by solving an inverse problem over the boundary voltages and measurements of the magnetic field (a).

The techniques discussed above cannot be translated to the tDCS application without changing the characteristics of the applied current (most were developed for alternating currents or AC). At the time of research, no technologies exist to visualize tDCS currents *in vivo*. The first aim of my PhD dissertation was to address this need. In the first Chapter, I discuss the theoretical

foundations of the approach developed, followed by experimental demonstration of its feasibility using a series of experiments with increasing complexity-from a tightly controlled artificial environment, to tDCS in simple biological tissue (human calf), to a typical tDCS setting. Our innovative approach also allows our technique to be integrated with fMRI (the subject of Chapter 3). When implemented, such a technique opens a new avenue to study tDCS at the systems level, providing a means to characterize the tDCS intervention as well as the brain's response *in vivo*.

Chapter 1: Establishing feasibility of visualizing tDCS currents *in vivo*

1. Methods

1.1 Theoretical framework to visualize tDCS currents *in vivo*: measuring current-induced magnetic fields using MRI

1.1.1 Physics of tDCS current induced magnetic fields

In classical electrodynamics, Maxwell's equations describe the generation and interaction of electrical and magnetic fields. In particular, Ampere's law (equation 1) describes that an applied electric current induces a magnetizing field:

$$\nabla \times \vec{H} = \vec{J} + \frac{\delta}{\delta t}\vec{D} \tag{1}$$

where $\vec{H}$ is the magnetizing field, $\vec{J}$ is the applied current density, $\vec{D}$ is the displacement field, t is time and ∇ is the curl operator. In a typical tDCS experiment using 1mA current, we expect magnetic field perturbations ≤ 1 μT to be induced. In an MRI, these perturbations are induced in a Tesla-strong static magnetic field environment. Under these conditions, it is appropriate to replace $\vec{H}$ according to

$$\vec{B} = \mu \vec{H} \tag{2}$$

where $\vec{B}$ is the induced magnetic field, and μ is the magnetic permeability of the biological tissue. Under the same conditions, μ is reported to be a scalar, varying on the order of ppm between tissues(69). By using Equation 2 in 1, we get:

$$\nabla \times \vec{B} = \mu\vec{J} + \mu\frac{\delta}{\delta t}\vec{D} \tag{3}$$

The time-varying term can be ignored for our DC case. Consequently, the induced magnetic field is directly proportional to the applied tDCS current density (along an orthogonal direction). A key point to note is that for the reported tissue μ, the relationship between applied current $\vec{J}$ and induced magnetic field $\vec{B}$ is linear. This linear relationship holds even if μ is a tensor. In fact, the independence of μ from $\vec{B}$ or $\vec{J}$ is a sufficient condition for linearity to hold.

1.1.2 Measuring tDCS current induced magnetic fields using MRI

Magnetic resonance imaging (MRI) is able to map changes in magnetic field along the MRI static field (B_z). Field disturbances perpendicular to B_z are generally invisible to MRI, as a consequence of the fact that (a) the B_z magnetic field is orders of magnitude larger than any typical disturbance and (b) magnetic fields add vectorially (Calculation shown in (70)). Using MRI field mapping, field variations along B_z can be measured as phase angles according to

$$\Phi_m = (\gamma \times \Delta B_z \times TE) \bmod (2\pi) \quad (4)$$

where Φ_m is the measured phase angle between 0 and 2π radians, γ is gyromagnetic ratio for protons in rads/sec (a constant), ΔB_z is the field deviation along B_z and TE is the echo time. A practical aspect of phase measurement is that phase angles outside $(0,2\pi)$ are mapped back onto this range causing a 'wrap' (represented by the modulo operation in equation 4). An acquired phase-map has to be unwrapped to calculate the correct phase to infer the underlying field.

Field mapping in fat tissue (a typical application in MRI) measures magnetic fields on the order of 3.35 ppm. In contrast, estimates using the Ampere's law show that a typical 1mA tDCS current, even when concentrated into traveling along a thin path, induces magnetic fields on the

order of 0.01 ppm 1 cm away. This calculation illustrates the primary challenge in measuring tDCS current-induced magnetic fields: a ~100-fold weakened SNR. Existing techniques to detect current-induced magnetic fields attempt to overcome the SNR impediment by boosting the 'signal', e.g., by increasing the current intensity and/or using time varying electric currents (~1Hz or higher)(62, 71, 72). This necessarily makes the characteristics of the applied current different from typical tDCS.

In contrast, our technique addresses the SNR limitation by statistically modeling out 'noise' sources and therefore is an imaging solution that does not constrain the applied current. In the proposed technique, a general linear model (GLM) is employed to model magnetic field maps using the applied-tDCS current as well as systematic noise sources (similar to linear regression analysis commonly used in fMRI). The magnetic field maps are acquired using the "#1" implementation, described next.

1.2 The "#1" Implementation

1.2.1 MRI protocol

To increase the efficiency of a general linear model in separating signal (i.e. the tDCS current induced magnetic field) from noise, the following MRI protocol was designed. As shown in Fig. 4, the MRI session consisted of 3 currents (repeated twice) and concurrent MRI field mapping scans. Before each scan, current was ramped up and maintained for 20 sec. The currents were applied in a pseudo random order, and interleaved with zero-current scans (a total of 13 field mapping scans per session). Two such sessions ('Active' and 'Sham') were included in an experiment, and the order of the sessions was counterbalanced across subjects (Fig. 4). Subjects were blinded to the nature of a particular session (single blinded design). During the 'Sham'

session, currents were ramped down back to zero before starting the MRI scan. In the Phantom experiment, an additional '–Active' session was included where the direction of the applied currents was reversed. In all other aspects, 'Active', Sham' and '–Active' sessions were identical.

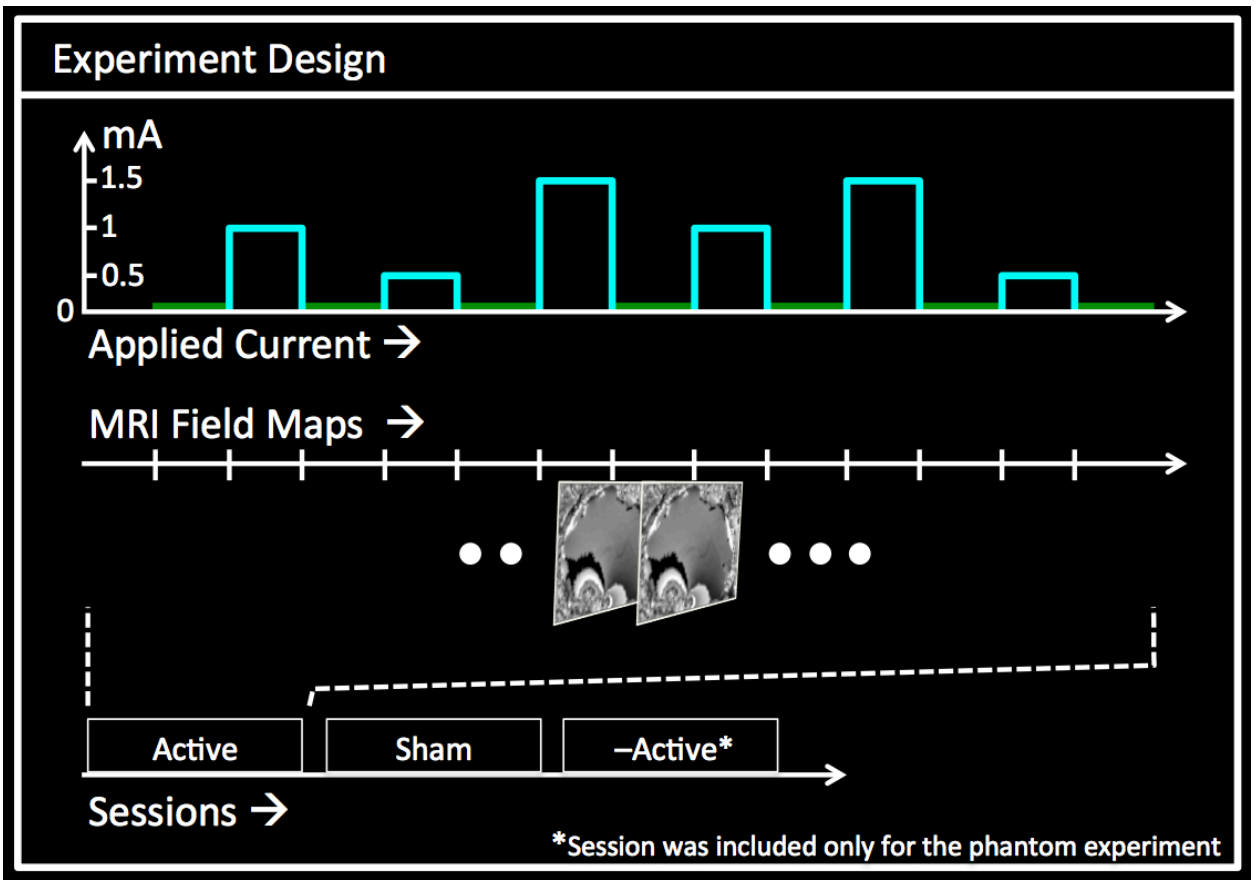

Figure 4. Experiment design and the MRI protocol for the "#1" implementation: Each MRI session consisted of 3 currents (repeated twice) and concurrent field mapping scans. Currents were applied in a pseudo random order, and interleaved with zero current scans. In the 'Sham'/ '–Active' sessions, the electric current was turned off/ was applied with reversed polarity, respectively.

1.2.2 MRI sequence: GRE

A 1mA current is typical in tDCS. The magnetic field induced by a 1mA current flowing through a long, thin wire 1 cm away is ~0.02 ppm (i.e. O(10) nT). Thus, even in the best case of no-noise, the induced magnetic field is 100 times smaller than the fields typically detected by

MRI (e.g. 3.35 ppm in fat tissue). This suggests that minimizing signal contamination should be a priority. As a result, a Gradient Recalled Echo (GRE) MRI sequence with (a) a long TR and (b) single channel coil was selected for data acquisition. With a long TR, contamination from stimulated echoes is minimized; and using a single channel coil minimizes potential phase contamination from combining images from multiple coils.

The sequence parameters of the GRE sequence were: TE_1/TE_2=4.92/14.76 msec, TR=1.15 sec, Matrix: 128 x128, BW=750 Hz/pix, FA = 25^0, 65 slices, 2x2x3mm^3 Voxel. For the calf experiment (described in 1.3.3), the flip angle, total slices and voxel size were adjusted to 65^0, 55 and 1.2x1.2x3 mm^3 respectively. It should be noted that MRI shimming was performed only once at the start of each session. Shimming is a pre-scan preparatory step that corrects for magnetic field deviations and may cancel out magnetic fields induced by tDCS currents. Potentially uncorrected field deviations, unrelated to tDCS, were explicitly modeled out.

The parameters TE_1 and TE_2 were selected as a compromise between sensitivity and ease of unwrapping phase. On the one hand, a large TE increases the noise and number of wraps, making unwrapping difficult. As can be seen from equation 4, the measured phase has to be unwrapped to calculate the correct phase to infer the underlying magnetic field. From the same equation, it can be seen that a low TE adversely impacts the magnetic field resolution i.e. the minimum detectable magnetic field. The minimum detectable field for the chosen TE_1 and TE_2 is 0.58 nT, adequate in light of the expected 10nT fields (calculation shown in 1.4.1.2).

1.3 Experiments

To establish feasibility of measuring magnetic fields induced by tDCS currents, three tDCS-MRI experiments were performed. In the first experiment, tDCS current induced magnetic fields were measured in the controlled environment of a phantom. Moving from this controlled environment towards a setting typical of tDCS interventions was the objective of the next two experiments. Thus, the second and third experiments investigated measurements in simple biological tissues (the human calf), and in healthy volunteers (head) respectively. Details of each experiment follow after a short description of the experimental apparatus developed to enable concurrent tDCS-MRI experiments.

1.3.1 Enabling concurrent tDCS-MRI experiments: Apparatus design and construction

Inter-modality interference poses the principal challenge to concurrent operation of tDCS and MRI. For instance, the current induced by quick gradient switching of MRI may interfere with the operation of tDCS. Additionally, the tDCS setup itself may passively introduce "third-party" signals that interfere with MRI operation. The different sources of interference, along with measures taken to minimize them, are described below:

1. Radio Frequency (RF) interference from outside the MRI scanner room:

   A principal design consideration for us was having the tDCS stimulator in the MRI control room, to enable the scanner operator to monitor the applied current. Such a setup required cables to carry the tDCS current from the stimulator (in the MRI control room) to the subject (in the MRI scanner). These cables can potentially introduce RF noise, picked up outside the scanner room. The RF noise is small enough to not pose a safety risk; however, it can still impact image quality. Consequently, quad-shielded coaxial cables were used to carry the

tDCS current from the stimulator, through the grounded MRI patch panel, to the subject in the MRI scanner. The shielding also mitigates distortion of the tDCS signal from MRI operation (discussed next).

2. Interference in tDCS from MRI:

MRI scanners utilize time varying magnetic fields for imaging. In accordance with Maxwell's equations, these fluctuating magnetic fields will induce a current on the loop formed by the current-carrying cables, electrodes and subject's head. The induced currents can potentially be hazardous, causing (i) brain stimulation outside the experimental design, and/or (ii) heating. In addition to being a safety hazard, (i) also introduces undesirable variance in the experimental measurements. Finally, the induced currents may also damage the tDCS stimulator.

Interference in tDCS from MRI was minimized as follows: First, the voltages induced by RF and gradient heavy MRI sequences were measured (open circuit measurement). These measurements were used to calculate resistor values that would dampen the induced currents to <10% of 1mA (a typical tDCS current). MRI compatible resistors of the calculated values were soldered between the cables and the electrodes. Additionally, a low pass RC filter was installed at the device end to protect the tDCS stimulator.

3. Interference in MRI from tDCS:

tDCS currents in the MRI scanner (a) will generate magnetic fields (in accordance with Ampere's Law), and (b) can generate electric currents in the gradient/shim coils (induction).

While (a) is expected and forms the basis of the imaging experiment, the DC nature, milliampere magnitude, and ramp times of ~O(10) seconds ensure that interference resulting from (b) should be minimal.

Last but not the least, means for independent and real-time monitoring of the applied current as well as the resistance across the subject's head were built into the designed apparatus. With this setup, tDCS MRI experiments could be performed safely, and with the necessary scientific rigor.

1.3.2 tDCS in a controlled environment (Phantom)

In order to evaluate feasibility of the proposed current mapping technique, a phantom was designed that channeled all applied current into a known path. The phantom was constructed by wrapping two U-shaped tubes ('A' and 'B' in Fig. 5a) around a cylindrical MRI phantom. The latter was a standard Siemens phantom (3.75g NiSO4 x 6H20 + 5g NaCl per 1000gm H2O, 0.5 Gallon, 10.6 cm diameter). Available in a sealed plastic container, its contents are insulated from external currents.

The current carrying 'A' tube (Fig. 5a) was a flexible plastic tube (ID=1/2 inch), wrapped around the long axis of the cylindrical phantom at its midline. The tube was filled with salt water (electrolyte), and fitted with copper electrodes at both ends. The tube 'B' was similar to 'A' (same material, electrolyte, 3/8 inch inner diameter), and placed at the distal end of the cylindrical phantom. The ends of tube 'A' were connected to the tDCS stimulator, whereas the ends of tube 'B' were open. Consequently, all applied currents were confined to tube 'A', with

current flow as shown by the pink dotted arrow in the figure. Tube 'B' served as a within-session 'control', carrying no applied current at any time.

With such a configuration, magnetic fields induced by applied currents can be intuited using Fleming's right hand rule (shown for the sagittal view, Fig. 5a). A quantitative estimate of the tDCS current induced magnetic field was also computed for comparison with experimental measurements (described below in 1.4.2.1). Using the "#1" implementation, experimental data was acquired for three sessions: 'Active', 'Sham' (applied currents set to zero) and '–Active' (direction of applied currents reversed).

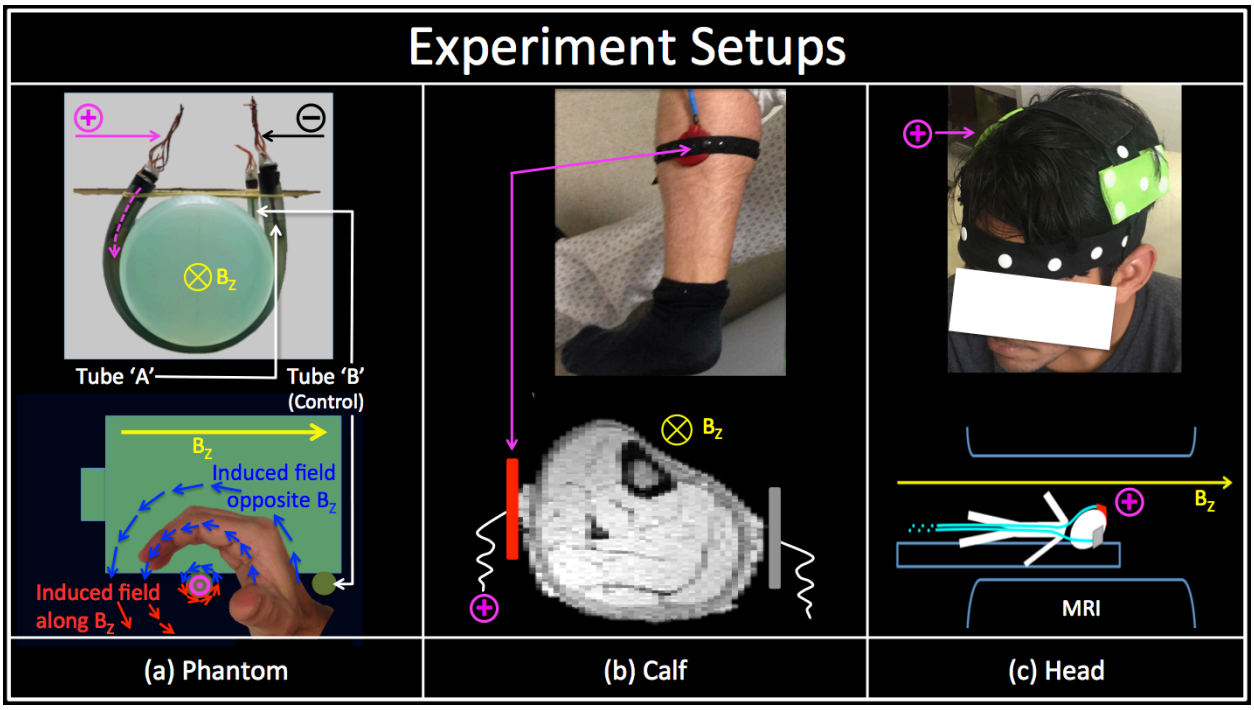

Figure 5. Setups for the (a) phantom, (b) calf-muscle, and (c) head-tDCS experiments: In the phantom, tDCS currents were confined to tube 'A', and the resultant magnetic fields as predicted by Fleming's right hand rule are shown in the sagittal view. Tube 'B' carried no current and served as an intra-session control. In the calf experiment, tDCS electrodes were placed laterally on the calf, as shown. A bilateral montage targeting the motor cortices (electrodes placed on C4(+)/C3(–)) was used in the head-tDCS experiment.

1.3.3 tDCS in a simple biological setting (calf-muscle)

The purpose of this experiment was to evaluate the proposed technique in an *in-vivo* setting involving relatively simple and electrically conductive biological tissues – a human calf. Fig. 5b illustrates the experiment setup. Round carbon rubber electrodes (2" inch diameter) were secured laterally on each side of the left calf. Conductivity gel (Cadwell, P/N# 202153-000) was used to ensure good electrical contact.

Similar to the phantom experiment, a quantitative estimate of the tDCS current induced magnetic field was computed based on a purely resistive finite element model for comparing with experimental measurements (details in 1.4.2.2 below). In-vivo experimental data was acquired from a single healthy subject (M) using the "#1" implementation for an 'Active' and 'Sham' session. Additionally, structural data for finite element modeling was acquired using a standard MPRAGE sequence (1 mm isotropic resolution).

1.3.4 Head tDCS (A typical tDCS setting)

The purpose of this experiment was to evaluate the proposed technique in a typical tDCS setting. The proposed technique was applied to healthy subjects receiving tDCS according to a bilateral montage targeting the motor cortices (anode/cathode on C4/C3, based on the 10-20 system, Fig. 5c). This montage was selected in particular because (i) it has been shown to generate reliable neurophysiological effects(2, 3) (and thus there is a high likelihood of electric currents penetrating into the brain parenchyma), and (ii) the overall direction of currents is perpendicular to the MRI static field (which is optimal for detection). Rectangular sponge electrodes (4.5x9cm) with their long axes in the A-to-P direction were used with the same conductivity gel as the calf experiment (Cadwell, P/N# 202153-000).

In-vivo magnetic field data was acquired using the "#1" implementation from 13 healthy subjects (Head: 7M, 29.7 ± 8.2 yrs; Calf: 1M, 36 yrs). For each subject, data was acquired for an 'Active' and 'Sham' session. Additionally, structural data was acquired using a standard MPRAGE sequence (1 mm isotropic resolution). Subjects were screened for neurological/psychiatric disorders. Written informed consent was obtained from all participants. The study was approved by the Institutional Review Board (IRB) at the University of California Los Angeles. All experiments and data acquisition were performed in accordance with the guidelines and regulations set by the Institutional Review Board (IRB) at the University of California Los Angeles.

1.4 Data Analysis

1.4.1 Experimental Measurements

1.4.1.1 Pre-processing

As described in previous sections, changes in magnetic field along the MRI static field (B_z) were measured as phase maps. Stochastic noise in a single voxel of the phase image is approximately zero-mean Gaussian for (magnitude) SNR ≥ 3 (73). A Gaussian noise is necessary for phase unwrapping as well as for GLM modeling of the preprocessed data (especially since at the other extreme of SNR=0, voxel noise in the phase image is uniformly distributed). The threshold of 3 is mathematically equivalent to a p-value (since the distribution of noise is known). This p-value threshold was adjusted (Bonferroni corrected) to account for the total number of voxels being tested, and voxels under the threshold were excluded.

Thresholded phase data was unwrapped using the Region growing algorithm implemented in the PhaseTools toolbox(74) (available as a plug-in for Fiji(75). Unwrapping was carried out at the individual volume level, followed by unwrapping within each slice. Next, SPM8 was used to realign image volumes to the first volume, to correct for inter-scan motion. The realignment parameters were estimated using the magnitude data from the first echo (TE_1). The realignment step was skipped for the phantom.

1.4.1.2 A General Linear Model (GLM) for measured phase

Measured phase was modeled as:

$$\Phi_m = \Phi_{Current}\big(TE, i(s)\big) + \Phi_{Drift}(TE, s) + \Phi_{Non-Current}(TE) + \Phi_0(s) + \Phi_{Noise} \qquad (5)$$

where Φ_m is the measured phase, $\Phi_{Current}$ is the phase due to current-induced fields, *TE* is the echo-time, "*s*" refers to the fact that the data is from the s^{th} scan and $i(s)$ is the current applied during the "*s*-th" scan. Φ_{Drift} is the phase due to inter-scan field-deviations caused by the time-varying drift of the main magnetic field, $\Phi_{Non\text{-}Current}$ is the phase due to field deviations unrelated to applied current but steady between scans (e.g. off-resonance), Φ_0 is the baseline phase, and Φ_{Noise} is the phase due to (Gaussian) noise.

The phase difference ($\Delta\Phi_m$) between the two TEs was computed. This step eliminates the baseline phase Φ_0. $\Delta\Phi_m$ was subsequently included as the dependent variable in a general linear model (GLM) with applied current ($i(s)$) as the predictor. This is based on the assumption that the current path remains the same for all applied currents. $\Delta\Phi_{Non\text{-}Current}$ by definition does not vary with applied current and is implicitly incorporated into the GLM intercept.

On the other hand, $\Delta\Phi_{Drift}$ was explicitly modeled by a polynomial function that was fitted least squares wise to phase measured during zero-current scans. This is consistent with the model for measured phase (equation 5) wherein the phase fluctuations for zero-current scans should be purely due to drift and noise. The degree (d*) of the polynomial was selected to optimally match the characteristics of the residual with those of Φ_{Noise} to prevent overfitting. Φ_{Noise} for each voxel was estimated using the magnitude image, as described in Gudbjartsson H. et al(73).

The regression coefficient for applied current obtained from the GLM analysis described above can be interpreted as the phase gained per 1mA applied-current. Using equation 4, this can be scaled to the induced magnetic field per mA of applied tDCS. The smallest magnetic field that can be detected provides a measure of the sensitivity of the "#1" implementation. Using a rearranged equation 4 (equation 6 below) and the fact that the full phase range of 0 to 2π radians is digitized into 4096 discrete levels in MRI, the smallest field that can be detected (unbiased) was determined to be 0.58 nT:

$$\Delta B_z = (Min.Angle) \times \frac{1}{\gamma \times \Delta TE} = \left(\frac{2\pi}{4096}\right) \times \left(\frac{1}{\gamma \times 0.00984}\right) \quad (6)$$

Here, ΔTE=9.84 msec (from the GRE sequence parameters), and γ is the gyromagnetic ratio for protons in rads/sec.

1.4.1.3 Statistical analysis

Obtained mA-current induced magnetic field maps were subsequently thresholded at $p < 0.05$ and cluster corrected (using AlphaSim(76) following standard statistical procedures for fMRI. For the head-tDCS experiment, an additional group level analysis was performed as

follows: current-induced field maps of individual subjects were coregistered to the corresponding structural images and subsequently normalized to the MNI space using SPM8. The normalized field maps were used to perform a one-sample t-test for both 'Active' and 'Sham' sessions. The obtained results were thresholded at $p < 0.05$ and cluster corrected for multiple comparisons using AlphaSim(76).

1.4.1.4 Region-of-interest analysis

Spherical ROIs of 1cm radius centered at projections of C3/C4 on the cortex(as reported by Vitali, P. et al.(77)) were constructed. Each ROI enclosed an equal number of voxels (178) following thresholding to exclude all out-of-brain voxels. $\Delta\Phi_{Current}$ within each ROI was averaged over all voxels, and subsequently used in a linear fit with applied tDCS current. The slope of such a fit can be interpreted as the ROI-averaged current-induced magnetic field. The calculated slopes for each ROI were used to perform a one-sample t-test for both 'Active' and 'Sham' sessions.

1.4.2 Simulations

1.4.2.1 Phantom

The current induced magnetic fields in the phantom were simulated as follows:

1. Magnetic field estimation

The current density at each point of the current carrying tube was estimated as described below. In such a case involving known DC current densities, the Biot-Savart law can be used to calculate current-induced magnetic fields:

$$B(r) = \frac{\mu}{4\pi} \iiint_V \frac{\vec{J} dV \times (\vec{r} - \vec{r}_V)}{|\vec{r} - \vec{r}_V|^3} \quad (7)$$

where $\vec{B}(\vec{r})$ is the magnetic field at the position $\vec{r}$, μ is the magnetic permeability, $\vec{J}$ and $\vec{r}_V$ are the current density and position vectors respectively of the finite volume element *dV*, and the integral sum is over the entire volume *V*. An implementation of the Biot-Savart law for line currents(78) was modified in-house and extended to volumetric finite element currents.

Magnetic fields (along B_z) over the 'sampled grid' were calculated as an average over fields computed on a 3D 'super-sampled' grid (Fig. 6a and b respectively, shown as 2D for simplicity). The averaging was done to model the fact that while MRI measurements represent the average magnetic field in a voxel, magnetic fields calculated using the Biot-Savart law estimate the field at a point and hold no information about the neighborhood. The sampled grid matches the resolution of the MRI experiment, and the resolution of the 3D super-sampled grid was 0.5 mm isotropic. The magnetic field value at each point was calculated using the Biot-Savart Law (equation 7).

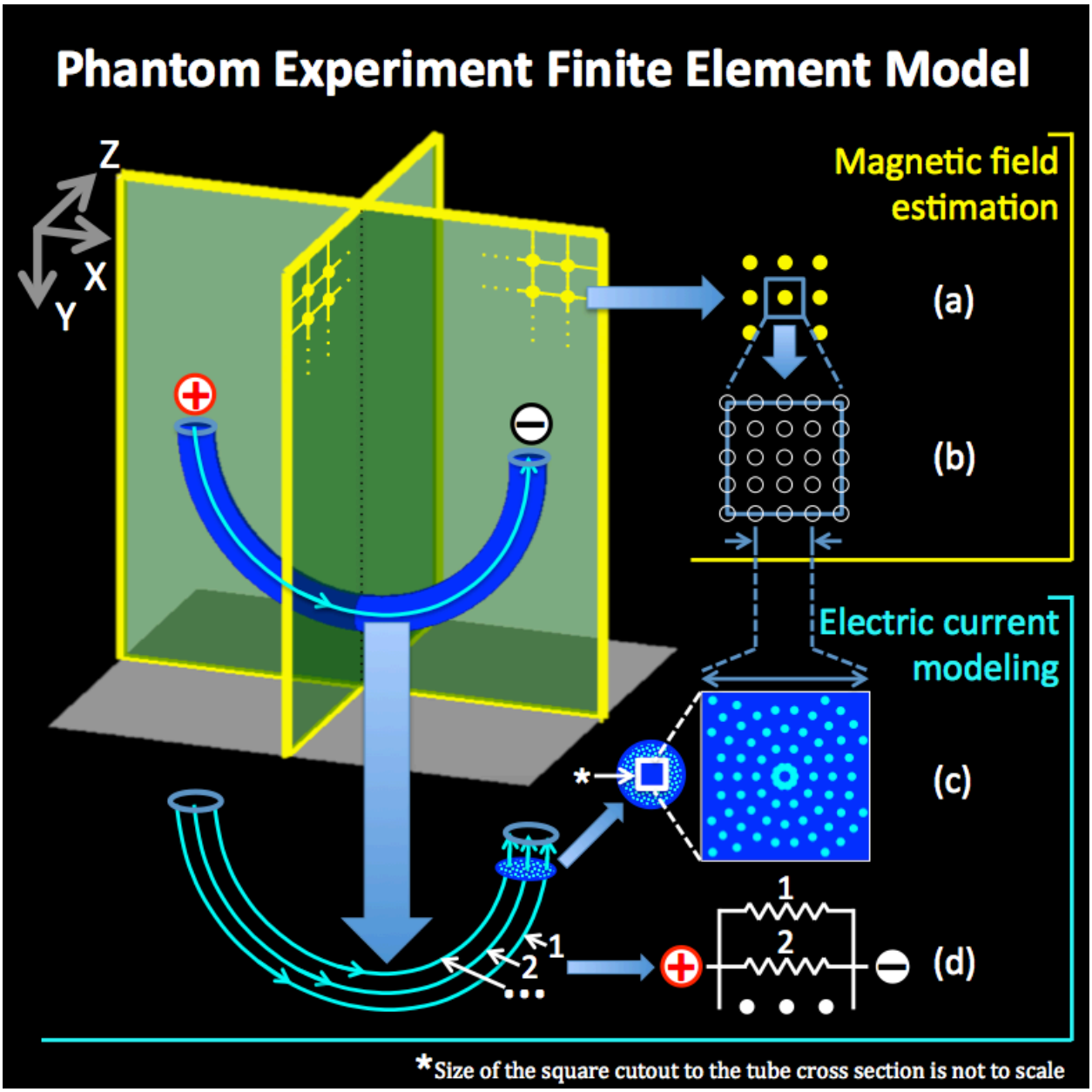

Figure 6. Finite Element Model used for simulations in the phantom experiment: Magnetic field at each point on the grid (a) was calculated as an average over points on the grid (b). The resolution of grid (a) was the same as that in experiments. Magnetic fields on grid (b) were calculated using the Biot Savart law, using current density finite elements (c). Current density values were calculated using the fact that the total applied current was 1mA, and the setup is electrically equivalent to a current divider circuit (d). Note that the calculation of current densities utilizes the geometry, and does not need the conductivity of the electrolyte.

2. Electric Current modeling

Assuming the salt-water electrolyte to be isotropic with uniform conductivity, the applied electric current is expected to travel in parallel 'streamlines' between the electrodes. Utilizing the

inherent symmetries in the system, these streamlines were discretized to a non-Cartesian grid as shown in Fig. 6c. The discretized grid had a spatial resolution of ~0.125mm isotropic. In other words, at least 64 points would be enclosed by the volume of a voxel on the "super-sampled" grid. The super-sampled grid is used to calculate magnetic fields, which are averaged down to the resolution of the "sampled grid"; the latter is the resolution of the experimental measurements.

Each streamline is an electric current flowing through an ohmic resistor. Thus, the system is electrically equivalent to a current-divider circuit (shown in Fig. 6d, with each branch of the circuit representing a streamline and the input being the total applied current. The resistance of each branch is equal to the resistivity of the electrolyte multiplied by the ratio of the length of the streamline to its cross-sectional area. While the length of a particular streamline is known from phantom geometry, the cross-sectional area is determined during the discretization process. The circuit was solved to compute the current through each streamline by choosing the total applied current to be 1mA. It should be noted that the conductivity of the electrolyte is not needed for this calculation. The choice of 1mA enabled direct comparison between the simulated fields and those detected using MRI (the latter being the induced magnetic fields per unit mA applied-current). The average current density within the conducting tube 'A' was 0.79 mA/cm^2 (1mA, ½ inch tube diameter).

1.4.2.2 Calf-muscle

Laplace's equation governs the voltage distribution in a purely resistive volume during constant current flow. Structural MR images of the calf were segmented into compartments

representing the gel, skin, fat, muscle and bone using a combination of automated and manual segmentation routines(44). The stimulation electrodes were imported as CAD models and positioned within the image data. Volumetric meshes were subsequently generated from the compartments (SIMPLEWARE Ltd, Exeter, UK) and imported to a commercial finite element solver (COMSOL Inc, MA, USA). Isotropic conductivity values were used (electrode: 5.99e7, gel: 1.4 S/m, skin: 0.465, fat: 0.001, muscle: 0.16, bone: 0.01) and the Laplace equation was solved to generate a spatial map of current density. The conductivity values used have been previously reported in Wagner et al.(79) (skin and bone) and Gabriel et al.(80)(muscle and fat).

The Biot-Savart law (equation 7) was used to calculate the current induced magnetic fields. The Biot-Savart law was implemented as a 3D convolution, as previously reported in Antal et al(81).

2. Results

2.1 Phantom experiment

Fig. 7a shows quantitative estimates of the current-induced magnetic field (computed using simulations) alongside experimental results of the 'Active' session (Fig. 7b, thresholded at $p < 0.05$, Cluster corrected $\alpha < 0.05$). As can be clearly seen, current induced magnetic fields detected by our technique are in close agreement with the simulation results ($r = 0.84$; $p = 3.8 \times 10^{-267}$; $N = 989$; cross-voxel correlation between slices shown in Fig. 7a and 7b). Fig. 7c shows the data from the 'Sham' session, where the current was switched off. As expected, no significant current-induced fields were detected. In the '–Active' session, the polarity of applied

currents was reversed (compared to 'Active'), which should result in a sign reversal of the induced magnetic fields while leaving the magnitudes intact (Ampere's Law, equation 3). The measured current-induced magnetic fields in the '–Active' session are consistent with this prediction ($r = -0.90$; $p = 2.3 \times 10^{-142}$; $N = 397$; cross-voxel correlation between slices shown in Fig. 7a and 7d).

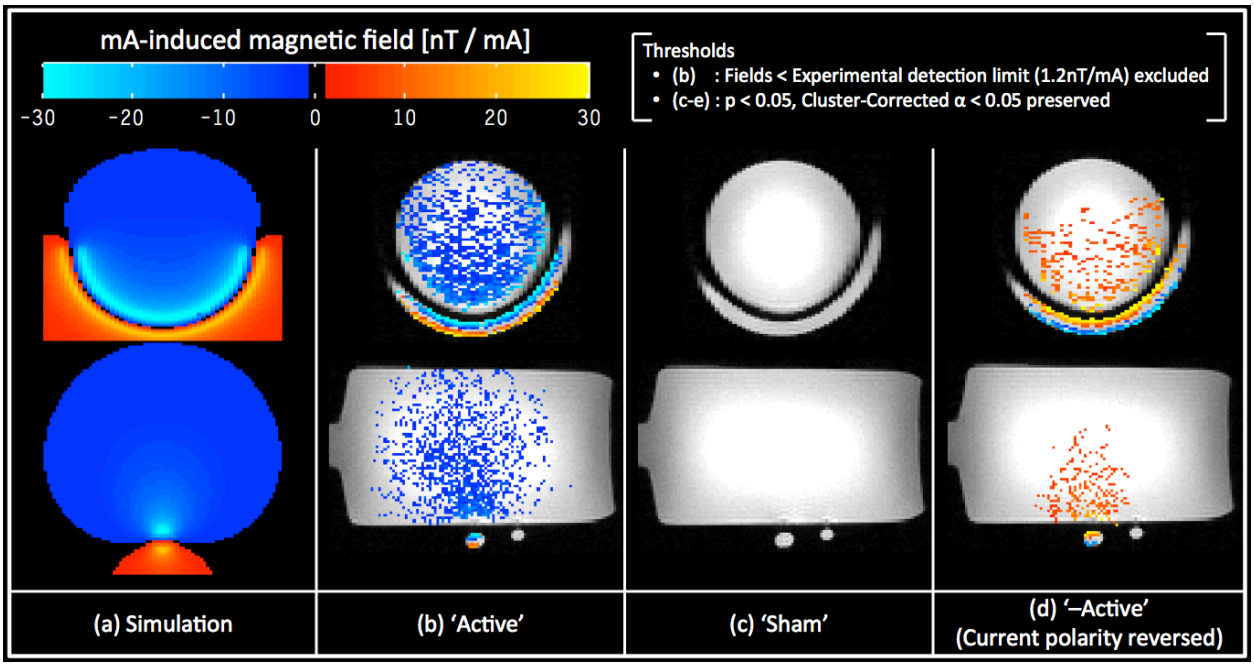

Figure 7. Phantom Experiment results: (a) shows the estimates from simulations, and (b), (c) and (d) show the significant tDCS current induced magnetic field (along B_z) measured in the 'Active', 'Sham' and '–Active' sessions. A significance level of $p < 0.05$, $\alpha < 0.05$ (cluster corrected) was used. The experimental results showed an excellent match with simulations ($r = 0.84$, and -0.90 for 'Active' and '–Active' respectively; and $p < 0.001$ for both)

Regions of interest (ROIs) consisting of the top (ROI1) and bottom (ROI2) halves of the current carrying 'A' tube (Fig. 8a) were selected from the same slice in all three sessions. Fig. 8b, c and d show the average measured fields within the ROI as a function of applied current for the 'Active', 'Sham' and '–Active' sessions respectively. Quantitatively, the measured fields per unit mA applied-current were found to be consistent with those calculated from simulations (by comparing slopes or β's of Fig. 8b, d with a). The magnitudes of estimated β's varied from ~10-

30nT/mA inside the current-carrying tube to 3-10 nT/mA inside the phantom. Qualitatively, the fields measured within ROIs were consistent with the following four predictions: (1) For the same session ('Active' or '–Active'), the current-induced fields should have opposite signs between ROIs, as can be intuited using Fleming's right hand rule (shown in Fig. 5a, Sagittal view). (2) For the same ROI, the current-induced fields should have opposite signs between 'Active' and '–Active' sessions, as predicted by Ampere's law (equation 3). (3) Current induced fields within ROI1 should be systematically higher than those of ROI2 because of the U-shaped geometry of the current carrying 'A' tube. Lastly, (4) there should be no detectable current-induced fields for the control 'Sham' session.

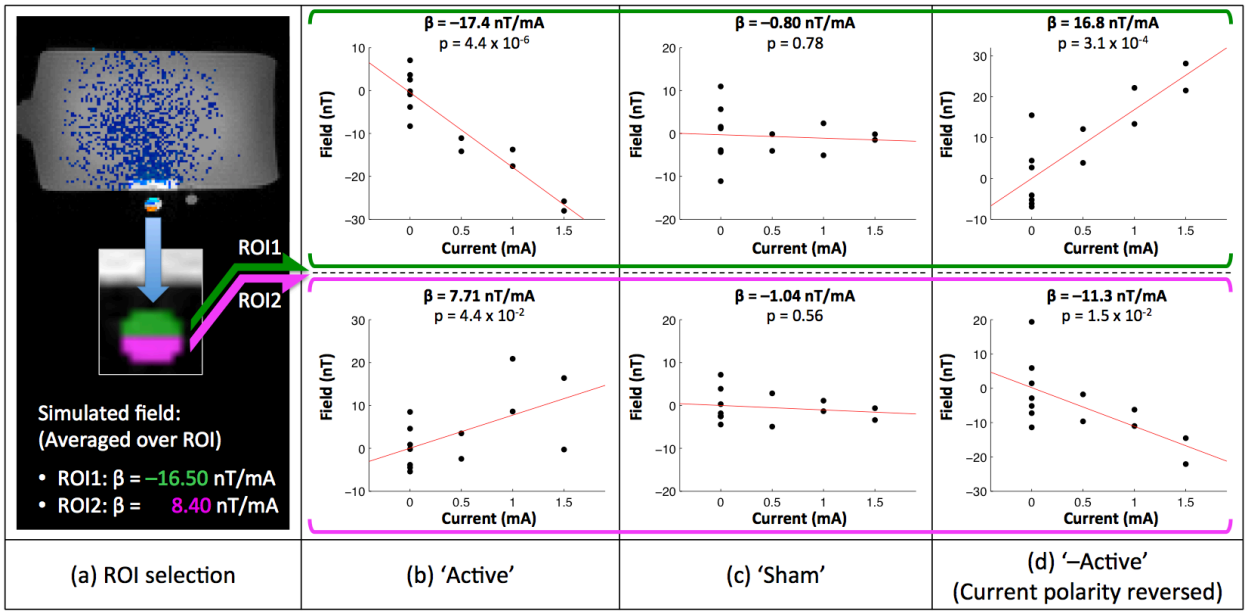

Figure 8. ROI analysis in the phantom experiment: As shown in (a), two ROI's were selected and the average tDCS current induced magnetic field was calculated for all sessions ((b)-(d)). The average fields matched well with the same predicted from simulations (compare β's). No significant fields were measured in the 'Sham' session (i.e. (c))

2.2 Calf experiment

Fig. 9a and b show the current induced magnetic fields (along B_z) measured for 'Active' and 'Sham' sessions respectively (thresholded to $p < 0.05$, Cluster corrected $\alpha < 0.05$). In the

'Active' session, magnetic fields close to the cathode electrode were observed to decrease with current while an increase of magnetic fields was observed on the ventral calf. No significant induced fields were detected for the 'Sham' session. Fig. 9c shows corresponding scatter plots for the two clusters (identified with an asterisk '*' in Fig. 9a). Measured current-induced fields were strongly correlated with the applied current in both clusters, with the magnitude of induced fields per unit applied-current in the range of 30-45 nT/mA.

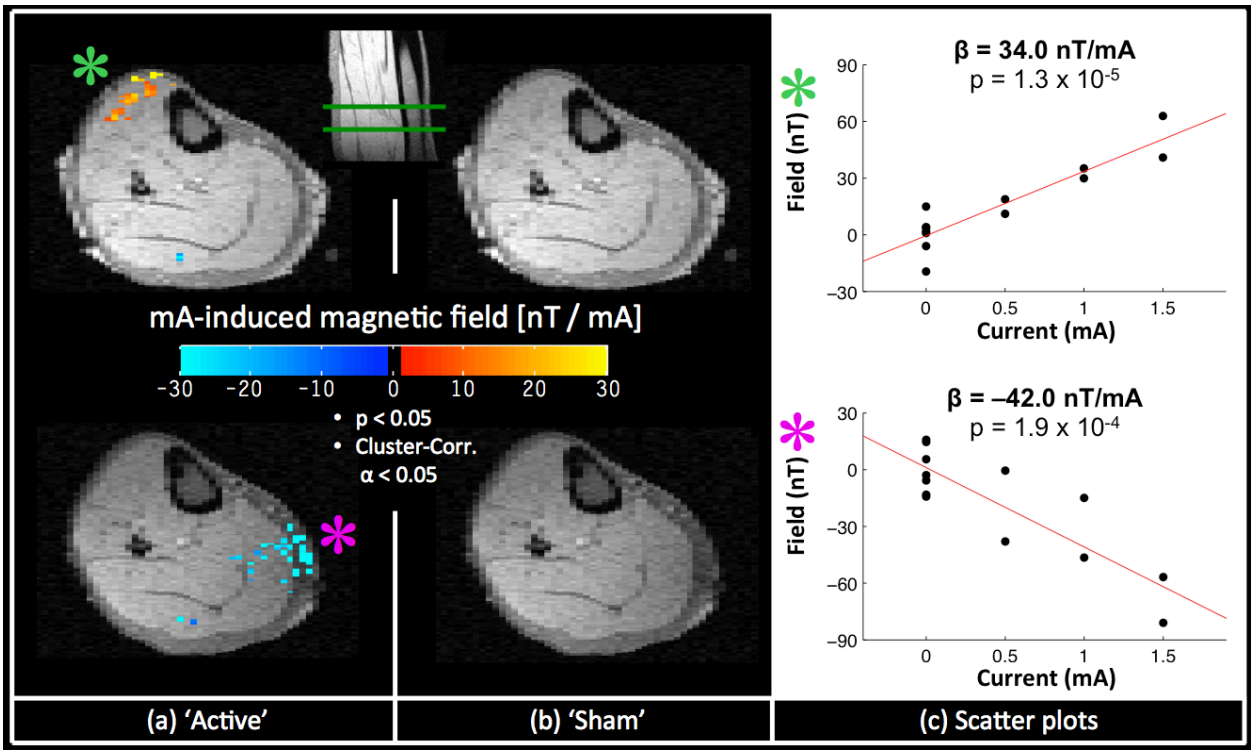

Figure 9. Calf experiment results: (a) shows the significant tDCS current induced magnetic field (along B_z) measured in the 'Active' session. A significance level of $p < 0.05$, $\alpha < 0.05$ (cluster corrected) was used. No significant fields were detected for the 'Sham' session (b). (c) shows scatter plots of the measured field with the applied tDCS current in two significant clusters (marker with '*' in (a))

Next, we compared measurements to simulations. In order to show the match between the experimental results and the simulated magnetic fields that are smooth in space, a more liberal threshold of statistical significance for the experimental data was used ($p < 0.1$ and Cluster corrected at $\alpha < 0.1$). As can be seen in Fig. 10, the measured magnetic fields match qualitatively

well with the simulated fields in terms of polarity (Spearman correlation between slices shown in Fig. 10: r = 0.43; p = 2.4 x 10^{-94};N = 2072 (middle row) and r = 0.20; p = 1.5 x 10^{-42};N = 4571 (bottom row)). However, spatial and intensity differences between the *in vivo* detected magnetic fields and its simulated counterpart were also observed. Lastly, no significant tDCS induced magnetic fields were detected for the 'Sham' session even with the more liberal threshold.

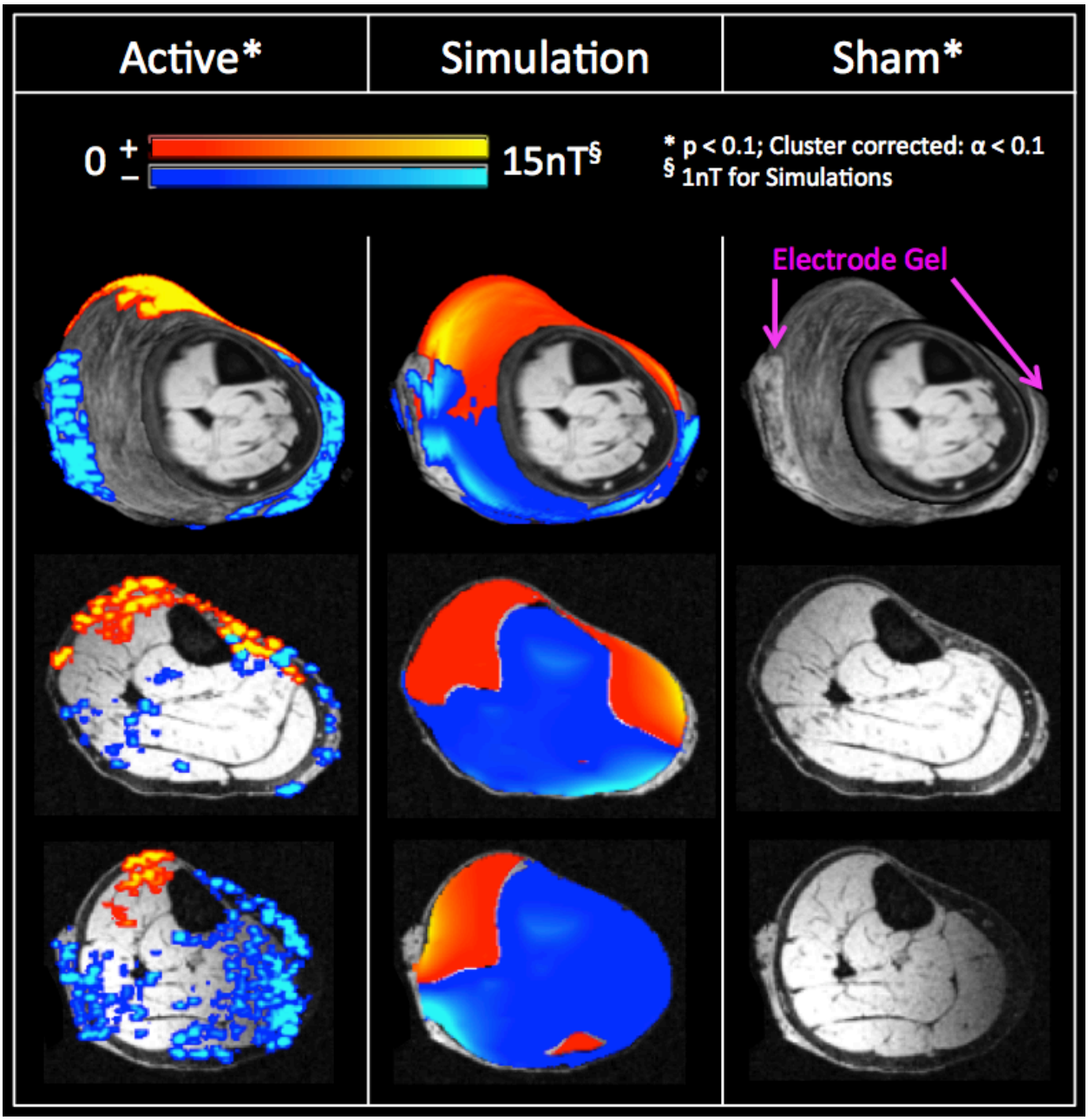

Figure 10. Comparing measurements ($p < 0.1$) with simulations in the calf experiment: Results from the 'Active', Simulations, and 'Sham' session are shown in columns 1,2 and 3 respectively. The 'Active' session matched qualitatively well with simulations (Cross-voxel Spearman correlations between simulated and 'Active' were 0.43, and 0.20; $p < 0.001$, for the middle and bottom slice respectively). No induced fields were observed in the 'Sham' session, even with the more liberal threshold.

2.3 Head experiment

Group level analyses identified consistently reduced magnetic fields (along B_z) at the left central sulcus under the cathode and in the precuneus region between the cathode and the anode electrodes (Fig. 11a). No significant current induced magnetic fields were observed for the 'Sham' session (Fig. 11b). Scatter plots (Fig. 11c) show the average induced fields as a function of applied current for the two significant regions. As can be seen from the plot, measured current-induced fields were negatively correlated with applied current, with the magnitude of the induced fields per unit applied-current in the range of 5-8nT/mA. The wider spread of data points, seen at 0mA (also seen in the calf and phantom scatter plots) is due to the fact that there were 7 measurements at 0mA versus 2 measurements at 0.5, 1 and 1.5mA respectively.

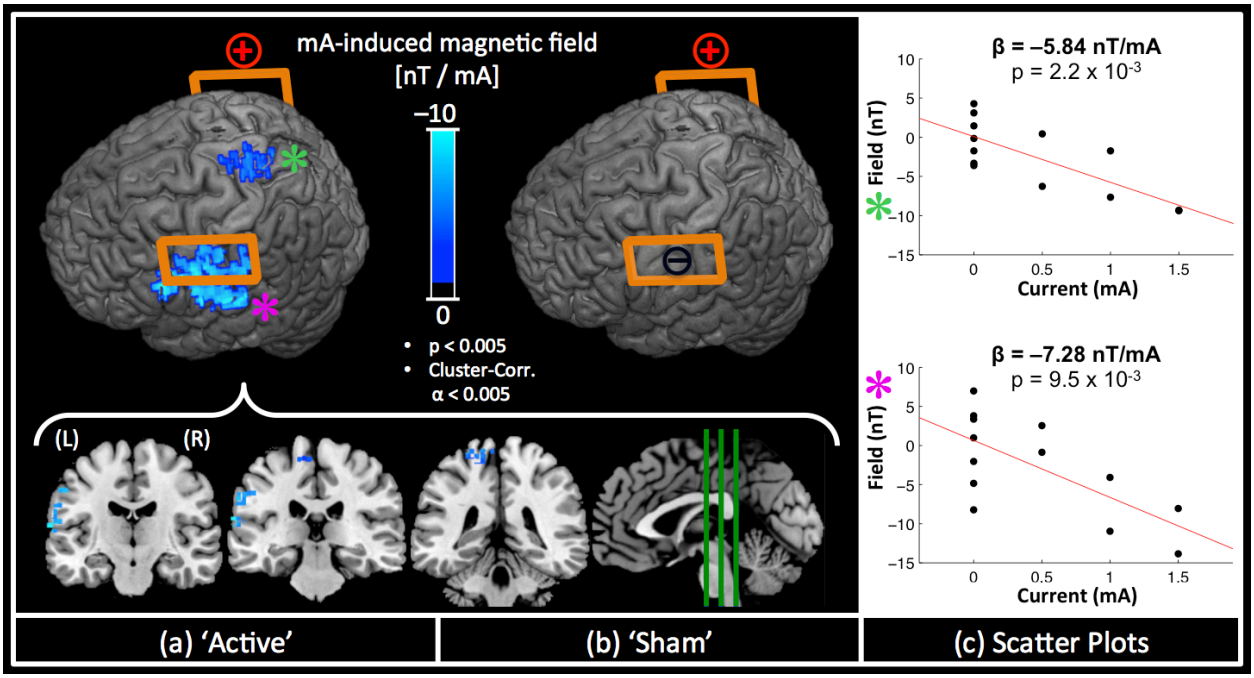

Figure 11. Head-tDCS results: (a) shows the significant tDCS current induced magnetic field (along B_z) measured in the 'Active' session at the group level. A significance level of $p < 0.05$, $\alpha < 0.05$ (cluster corrected) was used. No significant fields were detected for the 'Sham' session (b). (c) shows scatter plots of the measured field with the applied tDCS current in two significant clusters (marker with '*' in (a))

Although voxel-wise group analysis did not show significant magnetic field changes under or around the anode electrode in the 'Active' session, region-of-interest (ROI) analysis based on the cortical location of C3/C4 electrodes(77) revealed significant magnetic field reductions with applied tDCS current under both electrodes (Fig. 12, –6.1 nT/mA, –4.4 nT/mA; $p = 0.036, 0.044$; for C3/C4 respectively, N = 12 subjects, see Fig. 12). No such fields were detected for the 'Sham' session.

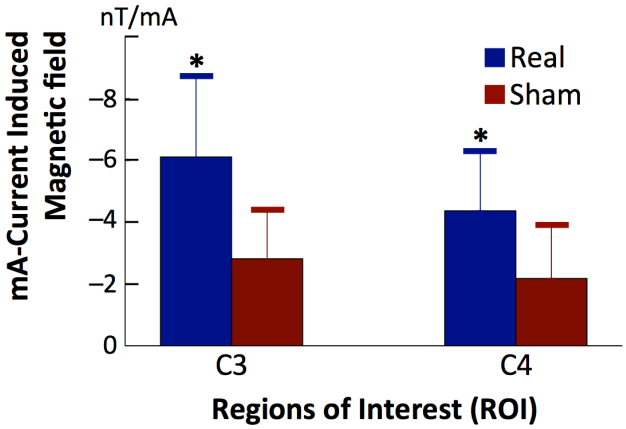

Figure 12. ROI analysis results in the head-tDCS experiment: Two ROIs, centered at cortical projections of the electrode positions (C4/C3) were used to calculate the average magnetic field induced per mA tDCS in each subject. A 1-sample t-test revealed significant magnetic field reductions in the 'Active' session ($\beta = –6.1$ nT/mA, –4.4 nT/mA; $p = 0.036, 0.044$ respectively). No significant fields were detected for the 'Sham' session ($\beta = –2.8$ nT/mA, –2.2 nT/mA; $p = 0.104, 0.233$ respectively).

3. Discussion

3.1 Feasibility and validity of the proposed technique

The key innovation of the proposed technique is that it provides quantification of magnetic fields directly induced by tDCS currents as a means to visualize target engagement.

This is in contrast to present *in vivo* imaging approaches that use surrogate markers to record the brain's responses to tDCS stimulation (e.g., BOLD/ASL fMRI(58, 60), MEG(82, 83) and EEG(84)). Feasibility was established through the phantom experiment where the measured current-induced magnetic field was in excellent agreement with simulations ($r = 0.84$, $p < 0.001$, $N = 989$). The phantom results also demonstrated excellent specificity as no significant magnetic fields were detected in either the within-session control (Tube 'B'), or during the control session ('Sham'). In its present implementation, our technique is capable of detecting fields as low as 0.58 nT at ~millimeter spatial resolution.

The limb experiment demonstrated *in vivo* feasibility of the proposed technique in relatively simple and electrically conductive biological tissue. While no field changes were detected during the 'Sham' session, magnetic field changes greater than 30nT/mA were observed during the 'Active' session. The experimental results also qualitatively matched the simulated in the human calf (Spearman $r = 0.43$, $p < 0.001$; $N = 2072$). Additionally, the signs of the detected magnetic fields are in accordance with Fleming's right hand rule applied to a model where the current density is largest at the skin. The latter is intuitive considering that subcutaneous fat behaves as an insulating sheath, with the ratio of electrical conductivities (skin:fat) being ~ 465. However, unlike the phantom experiment, the magnitude of the detected fields was found to be greater than the simulated fields. This difference could be due to heterogeneity in the tissue conductivity or complicated boundary conditions, leading to potential "hotspots" of electromagnetic fields. These observations highlight the need for reliable *in vivo* mapping of electromagnetic fields even for organs and limbs with relatively simple biological compositions.

Finally, we performed measurements in a typical tDCS setting, using a bilateral M1 montage on 12 healthy volunteers. A group level analysis revealed relatively weak (5-8nT/mA) yet statistically significant magnetic field reductions around the central sulcus (underneath the cathode) as well as in the precuneus region (around mid-way between the electrodes). Our observations are consistent with modeling studies that have predicted peak current densities to exist under the electrodes(42), and for large electrodes (25-35 cm^2) less than 10 cm apart, a single peak current density to exist between the electrodes(85). Moreover, the magnitude of the experimentally detected fields, 0-10nT/mA, was found to be the same order as that of simulated fields reported in a recent study(81) (although the study used a different cathode positioning). Furthermore, although significant field changes were not detected under or around the anode in voxel-wise group analysis, an ROI analysis revealed significant field changes under both electrodes (and none during Sham). These field changes were also observed to have the same sign; which is intuitive given that the direction of tDCS current flow is the same (from anode to cathode) at both electrodes. However, it is not clear why the field changes were more significant under cathode than anode in our experiment. One potential explanation is the relatively large electrode size making the induced electromagnetic fields "diffuse", and such an effect may be asymmetric between anode and cathode. With improved sensitivity of our technique (see future developments below) and improved focality of tDCS montage (e.g., high-definition tDCS(48)), such hypotheses will be evaluated in future studies.

3.2 Advantages of the proposed approach to visualize tDCS currents *in vivo*

The proposed approach for visualizing tDCS target engagement through its induced magnetic fields is appealing since the magnetic field is directly induced by and linearly proportional to the applied current (as described by Ampere's law, equation 3). Moreover, the physical constant involved in the relationship between magnetic field and direct current is highly stable across biological tissues (variation of magnetic permeability is on the order of ~ppm(69)). In contrast, existing experimental techniques use surrogate markers of the brain's response to tDCS stimulation (e.g., BOLD, ASL, EEG, MEG(58, 60, 82-84)). These represent a secondary response to the applied stimulation, and may extend beyond the site of stimulation due to brain networks. Additionally, unlike the physical relationship between magnetic fields and applied current, the relationship between these markers and the applied tDCS current is complicated, and not easy to interpret.

In applications involving milliampere currents, the primary challenge for detecting current-induced magnetic fields is the weak signal relative to noise (SNR). Existing techniques to detect weak magnetic fields attempt to overcome the SNR limitation primarily through enhancing the 'signal', e.g., by increasing the current intensity and/or using time varying currents (~1Hz or higher)(62, 71, 72). In contrast, the proposed technique addresses the SNR limitation by statistically modeling out a range of 'noise' sources (using the linear relationship between applied-current and induced magnetic fields), and is thus able to detect small magnetic fields with high sensitivity and spatial resolution.

In the proposed technique, a general linear model (GLM) was employed to model a set of magnetic field maps with applied current as well as systematic noise sources, similar to linear

regression analysis commonly used in fMRI. The choice of a GLM is supported by the fact that the relationship between applied current and measured magnetic field is linear (Ampere's Law, equation 3), and by ensuring the distribution of stochastic-noise to be Gaussian. Another advantage of using a GLM is that many statistical methods developed for fMRI can be adapted for the proposed technique. The use of a GLM does assume (implicitly) the invariance of current path with different intensities of applied currents. This assumption is reasonable considering the small magnitude of currents used (will not induce neuronal discharge) and the fact that all currents were applied in the same direction.

3.3 Limitations and future developments

It should be noted that the proposed technique only maps the magnetic field changes along B_z. In the absence of additional information, mapping electric current requires measuring all three spatial components of the induced field. One possible solution is to map the induced fields of a subject in at least three different orientations, which may be feasible with an open magnet. Alternatively, constraining computational current prediction models with a single experimentally verified component of the induced field could improve the accuracy for predicting current distribution.

In the present study, we were able to visualize tDCS current-induced magnetic fields in human brains at the group level. This is a significant first step to experimental verification of target engagement. In addition to verification, our technique can also help advance focal stimulation, shown to be more efficient than conventional tDCS(8), in the following way: By identifying group-wide peak-intensity areas from imaging studies (performed for conventional

tDCS), our technique can potentially (a) provide target engagement confirmation for a conventional tDCS trial; and if treatment effects are observed, (b) identify target sites for future studies with focal stimulations with a reasonable expectation of the same treatment effects.

4. Conclusion

This chapter demonstrates the feasibility of measuring magnetic fields induced by tDCS electric currents *in vivo*. However, the "#1" implementation utilized in experiments was unable to detect tDCS current induced magnetic fields in individual subjects. The capability to reliably map fields in individual subjects would allow us to (1) overcome the potential averaging effects of a group analysis, given the variability of cortical geometry and current distribution across subjects, (2) compare with computational models, and (3) assess target engagement in individual subjects. As a result, addressing this limitation became the focus of subsequent research. The next chapter will discuss how analysis of this limitation was used to inform the development of the state of the art implementation, which could detect current induced magnetic fields in individual subjects.

Chapter 2: State of the art: Visualizing tDCS currents in individual subjects

1. Study rationale

1.1 Visualizing tDCS currents: Capabilities of the previous "#1" implementation

In the previous Chapter, a novel MRI-based approach for direct visualization of the tDCS current by measuring the current induced magnetic fields is described. This approach was implemented as "#1", and three experiments were performed to assess the feasibility of the approach and the capabilities of the implementation. In the first experiment, current-induced magnetic fields of ~15nT/mA were measured in a specially designed phantom. These measurements were compared with simulations, and were found to be a solid match ($r = 0.84$, $p < 0.001$). The experimental data also demonstrated excellent specificity as no current induced magnetic fields were detected in the control session ('Sham'), or the intra-session control (Tube 'B', Fig. 2a). Similar results were obtained in the second experiment, performed on structurally simple biological tissue (the human calf). Consequently, it was concluded that the proposed approach of measuring tDCS current induced magnetic fields (along B_z) was feasible. However, the implementation utilized (i.e. "#1") had an important limitation, described below.

1.2 Principal limitation: Detection in individual subjects

In the final experiment with the "#1" implementation, current induced magnetic fields were detected in a typical tDCS montage at the group level. However, we were unable to detect the same fields reliably in individual subjects. Although group level results can be used to

visualize tDCS currents *in vivo*, detection in individual subjects is ideal, since it would enable one to (1) overcome the potential averaging effects of a group analysis, given the variability of cortical geometry and current distribution across subjects, (2) compare with computational models, and (3) assess target engagement in individual subjects. As a result, the inability to detect tDCS current induced magnetic fields in individual subjects was considered to be the principal limitation of the "#1" implementation. Addressing this limitation to enable measurements in individual subjects was the second aim of my PhD dissertation, and the focus of research described in this chapter.

2. Methods

2.1 Addressing the principal limitation of "#1"

2.1.1 Root-cause: Insufficient Signal-to-noise (SNR)

The principal limitation of the "#1" implementation was the inability to detect tDCS current induced magnetic fields in individual subjects. However, the fact that detection was successful in the phantom and calf experiments suggests that this limitation is a shortcoming of the implementation rather than the overall approach. Moreover, the observation that the magnetic fields detected in the head (~7nT/mA, albeit at the group level) are smaller than those detected in the phantom/calf experiments (~15nT/mA) indicates that this limitation is caused by insufficient signal relative to noise (SNR).

2.1.2 Improving SNR: The noise reduction approach

SNR can be improved by increasing signal and/or reducing noise. It is useful at this point to think of signal and noise separately since they can be adjusted independently, as shown in equation 8 (derived from equation 4 by splitting Φ_{meas} into Φ_{true} and Φ_{noise}).

$$B_{z,\text{meas}} = \underbrace{B_{z,\text{true}}}_{\substack{\propto i_{tDCS}\,; \\ by\ Ampere's\ Law}} + \frac{\Phi_{\text{noise}}}{\gamma \times TE} \tag{8}$$

Here, $B_{z,\text{meas}}$ is the measured magnetic field, and the right-hand side terms are the 'signal' ($B_{z,\text{true}}$) and 'noise' respectively. In particular, Φ_{noise} is the noise in the phase measurement, γ is the gyromagnetic ratio for protons and TE is the echo-time. By Ampere's Law, the signal, $B_{z,\text{true}}$, is directly proportional to the tDCS current. Thus, any improvement in signal to increase SNR has to necessarily alter the tDCS current characteristics, which is not ideal for tDCS research.

In contrast, the noise term in equation 8 does not depend on the applied current, and as a result, measures for noise-reduction impose no constraints on tDCS stimulation. In fact, noise-reduction measures would only require a modification of imaging parameters (e.g. an increase in TE). This makes noise-reduction strategies particularly well suited to improve SNR in our tDCS application. The following sections describe how sources of noise were identified and attenuated to improve SNR.

Parameters affecting noise: intrinsic-noise (σ), total number of measurements (N) and echo time (TE)

Equation 8 contains an expression for noise present in a single measurement. Since our technique uses multiple measurements in a general linear model (GLM) for estimation, equation 8 needs to be modified to include the GLM term:

$$\begin{aligned} \mathrm{Noise}\left(\mathrm{B_{z,meas}}\right) &= \frac{\Phi_{\mathrm{noise}} \times \sqrt{\{(X^T X)^{-1}\}_{i,i}}}{\gamma \times \mathrm{TE}} \\ &\sim \frac{\Phi_{\mathrm{noise}}}{\mathrm{TE} \times \sqrt{N}} \end{aligned} \tag{9}$$

Here, X is the model-matrix of the general linear model, *i* is the index to the column of X containing applied-tDCS current values, N is the total number of measurements, and the rest of the terms are as defined earlier. As can be seen from the equation, an increase in the number of measurements (i.e. "N") reduces noise in the $\mathrm{B_{z,meas}}$ estimate. The overall impact of an increase in $\sqrt{N}$ can be understood as an SNR boost through an increase in statistical power.

We next consider the case of the random variable Φ_{noise}. Φ_{noise} follows a zero-mean Gaussian distribution for $A/\sigma \geq 3$; where A is the amplitude of the signal in a voxel, and σ is the standard-deviation of noise in a single measurement. Note that A is closely related to the measured magnitude signal, as described in Gudbjartsson H. et al.(73) Noise being Gaussian allows the "N" measurements to be used directly in a GLM. In particular, the variance of this Gaussian distribution is σ^2/A^2, suggesting that attenuating σ (e.g. using better receiver coils) should reduce noise in the magnetic field estimation. Incorporating this into equation 9 along with the fact that A decays with TE (T2/T2* decay), we get:

$$\text{Noise}\left(B_{z,\text{meas}}\right) \sim \frac{Gaussian\left(0, \frac{\sigma}{A}\right)}{\text{TE}\times\sqrt{N}} \quad \text{subject to } \frac{A}{\sigma} \geq 3 \text{ and } A \downarrow \text{as TE} \uparrow \tag{10}$$

With equation 10, we can finally consider the case of TE. Because A decays with TE, the $A \geq 3\sigma$ constraint puts an upper bound on TE. Additionally, increasing TE also increases the variance of the Gaussian term thereby mitigating some of the reduced noise. Consequently, there exists a limit on how much noise can be decreased by increasing TE.

In summary, equation 10 illustrates three different parameters that can be used for attenuating noise– (1) σ, or the intrinsic noise in a single measurement; (2) N, or the total number of measurements; and (3) TE, or the echo time (to an extent). A benefit of increasing TE is the improved sensitivity, i.e. the minimum magnetic field that can be detected (as shown by equation 6).

Reevaluating implementation choices: Single vs. Array Coils (σ) and GRE vs. EPI sequence (N, TE)

The "#1" implementation utilized a single-channel coil, a GRE-sequence with a long TR (resulting in scan duration of 2.5 minutes) and a TE of at most 14.76 msec. At the time, these choices were made to minimize contamination of the phase signal due to stimulated echoes and phase-wraps. Preventing signal contamination is important, since the tDCS current induced magnetic field signal is two orders of magnitude smaller than signals typically measured by MRI (~0.01ppm vs. 3.5ppm for fat).

However, the "#1" implementation was found to provide insufficient SNR for detection in individual subjects. Going forward, three implementation parameters that could be used to improve SNR were identified, namely (1) σ, or the intrinsic-noise in a single measurement, (2) N, or the number of measurements and (3) TE, or the echo time. Based on these parameters, the "#1" implementation was reevaluated as described below.

(1) Improving σ: Using multi-channel coils instead of implementation "#1"'s single-channel coil would directly improve the intrinsic noise. However, the acquired multi-channel data needs to be recombined into a single image, which introduces phase-wrap errors. In pilot experiments, it was found that these errors could be avoided by using the sum-of-squares algorithm for image reconstruction.

(2) Improving 'N': A long TR minimizes phase-signal contamination from stimulated echoes. The GRE sequence of the "#1" implementation uses a long TR, but at the cost of a 2.5 minute scan duration. The latter limits the number of measurements (i.e. 'N') that can be performed in a MRI session. In comparison, an Echo Planar Imaging (EPI) sequence is more time-efficient, acquiring whole brain data in seconds. However, the EPI sequence introduces its own set of phase-errors. Theoretically, these phase-errors are expected to be consistent across measurements, and thus should be removable (as the intercept in the general linear model).

(3) Increasing 'TE': As described in the previous section, a long TE improves SNR (to an extent) as well as the sensitivity of the proposed technique. However, longer TEs create more phase-wraps in the acquired image. This problem is compounded by a larger 'N': for instance,

switching from a GRE to an EPI-based implementation presents a change in scan-duration from 2.5 minutes to 4 seconds, which is a ~40x increase in the number of images to be unwrapped. To address this, a semi-automatic technique based on the Region growth algorithm implemented in PhaseTools(74) was developed in-house. This technique made the unwrapping of large phase-datasets feasible, enabling the improvement of the previous implementation from {TE=14.76 msec, N=13} to {TE=26 msec, N=540}.

2.2 State of the art: The "#2" Implementation

Incorporating all three means of improving SNR discussed in the previous section, the "#2" implementation utilizes a 12-channel array coil, EPI sequence and a longer echo time to detect tDCS current induced magnetic fields. Additionally, the "#2" implementation also utilizes the magnitude of the measured signal to measure the brain's response to stimulation (the subject of the next chapter). Exact details of changes with the new implementation (including the MRI protocol as well as post-processing changes) are described below.

2.2.1 MRI protocol

Similar to "#1", the MRI protocol of the "#2" implementation was designed to take advantage of the linear relationship between the applied tDCS current and the induced magnetic field. Thus, four distinct tDCS currents (0, 0.5, 1, 1.5 mA) were applied in a pseudo-random order during a MRI scan (Fig. 1). Each current was applied for 2.5 minutes, with a 30 second ramp time; and subjects were blinded to the strength of the current being applied. Magnetic field data was acquired from three such back-to-back scans.

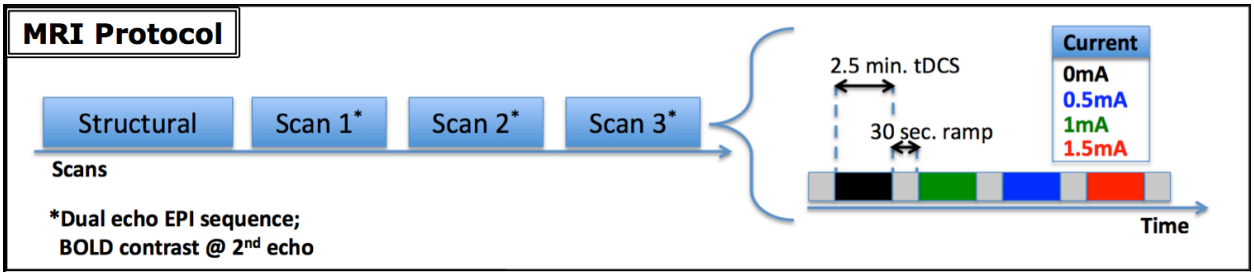

Figure 1. MRI protocol in the "#2" implementation: A dual echo EPI sequence was used to collect magnetic field mapping data using three back to back scans. During each scan, current intensities of {0, 0.5, 1, 1.5 mA} were applied in a pseudorandom order for 2.5 minutes each, with a 30 second ramp time. Additionally, structural data was acquired using a MPRAGE sequence. The second echo of the acquired magnitude data contained the BOLD contrast, analysis of which is the subject of Chapter 3.

2.2.2 MRI sequence: Dual echo EPI

A dual-echo EPI sequence was used to acquire phase data in the "#2" implementation. Data was acquired from two echoes to enable subtracting out the baseline phase, similar to the approach used in Chapter 1. The EPI sequence also incorporated measures to increase SNR, namely, a higher TE (TE_2 = 26 msec, ΔTE = 15 msec vs. $\Delta TE \sim 10$ msec previously), higher 'N' (N = 540 vs. 13 previously), and acquisition using a 12-channel coil. The sequence parameters of the dual-echo EPI sequence were TE_1/TE_2=11/26 msec, TR=4 sec, Matrix: 64 x64, BW=3000 Hz/pix, FA = 90^0, 24 slices, 3.44 x 3.44 x 5mm^3 Voxel, 7/8 Partial Fourier, with sum of squares reconstruction to combine signals from individual coil elements.

2.2.3 Post-processing changes

In addition to a different experimental design and MRI sequence, the "#2" implementation also included changes in postprocessing. In brief, these were (a) a faster and more efficient technique for phase unwrapping, (b) a different technique for correcting magnetic field-drift, and (c) an improved GLM to model the acquired data. (Details are in the Data Analysis section, 2.4.1).

2.3 Experiments

Experiments were performed to detect tDCS current induced magnetic fields in individual subjects. In-vivo data was acquired from 7 subjects (4M, 23.1 ± 6.6 yrs) using the "#2" implementation. Subjects were screened for neurological/psychiatric disorders. Written informed consent was obtained from all participants. The study was approved by the Institutional Review Board (IRB) at the University of California Los Angeles. All experiments and data acquisition were performed in accordance with the guidelines and regulations set by the Institutional Review Board (IRB) at the University of California Los Angeles. During acquisition, each subject was asked to stay awake and fixate on a cross (white on black background). Additionally, a standard MPRAGE sequence with 1mm isotropic resolution was used to acquire structural data for simulations.

The same tDCS montage as the head-tDCS experiment (in Ch-1) was employed in the tDCS-MRI scans. In brief, tDCS was delivered using a bilateral montage, with anode/cathode placed on C4/C3 respectively (shown in Ch-1, Fig. 2(c)). The electrodes were rectangular (4.5x9cm) in shape with their long axes in A-P direction. Conductivity gel (Cadwell, P/N# 202153-000) was used to ensure good electrical contact between scalp and electrodes. In addition to the reasons described previously for using this specific montage (Ch-1, 1.3.4), using the same montage as before enables a direct comparison between the two implementations.

2.4 Data Analysis

2.4.1 Experimental Measurements

2.4.1.1 Pre-processing

The acquired experimental data was preprocessed in a manner similar to that of the previous implementation. First, voxels with non-gaussian phase noise were excluded using a Bonferroni-based statistical technique (as described in Ch-1 1.4.1.1). Next, phase unwrapping was carried out slice-wise, for each TE, using an improved in-house technique based on the PhaseTools(74) toolbox in Fiji(75). The in-house improvement was necessary, given the substantial increase in the size of the dataset (540 volumes vs. 13), as well as the number of phase wraps in each volume (because of the higher TE). Finally, SPM8 was used to realign image volumes to the first volume, to correct for inter-scan motion. Realignment parameters were estimated using magnitude data from the first echo (TE_1).

2.4.1.2 An improved General Linear Model (GLM) for measured phase

Image volumes from the three back-to-back MR scans were concatenated, and the measured phase was modeled as:

$$\Phi_m = \{\Phi_{Current}(TE, i(s)) + \Phi_{Drift}(TE, s) + \Phi_{Non-Current}(TE) + \Phi_0(s) + \Phi_{Noise}\} + \Phi_{Motion}(s) + \Phi_{Scan}(S(s)) \quad (11)$$

where curly brackets indicate terms present in the previous version of the GLM (Ch-1, 1.4.1.2). Here, Φ_m is the measured phase, $\Phi_{Current}$ is the phase due to the current-induced magnetic fields, *TE* is the echo-time, "*s*" refers to the fact that the data is from the s^{th} image volume, *i*(*s*) is the current applied during acquisition of the "*s*-th" volume and S is the MRI scan during which the s^{th} volume was acquired. Thus, for the "#2" implementation that uses 3 back-to-back scans, S is 1,2 or 3. Φ_{Drift} is the phase due to the time-varying drift of the main magnetic field, $\Phi_{Non\text{-}Current}$ is the phase due to field deviations unrelated to applied current but steady between scans (eg. off-

resonance), Φ_0 is the baseline phase, Φ_{Noise} is the phase due to (Gaussian) noise, Φ_{Motion} is the phase associated with subject motion and Φ_{Scan} accounts for phase offsets across different scans.

Φ_{Drift} was modeled out by fitting a 2nd degree polynomial to Φ_m for each MRI scan. Next, the drift-corrected data was modeled using a GLM wherein the applied current was included as a predictor (implicitly assuming that the current path remains the same across applied currents). Uncorrected residual drift was modeled out by including the global mean-phase in the GLM. $\Phi_{Non\text{-}Current}$ by definition does not vary with applied current or between scans, and is implicitly modeled by the GLM intercept.

In the previous version of the GLM, fluctuations in Φ_0 were eliminated by using the phase difference between the two TEs (i.e. $\Delta\Phi_m = \Phi_{m,\,TE2} - \Phi_{m,\,TE1}$). However, employing the phase difference has two drawbacks: first, it increases overall noise since the noise-variances of $\Phi_{m,\,TE1}$ and $\Phi_{m,\,TE2}$ (both gaussian distributed) add up. Second, using the phase difference results in a decrease in sensitivity (reported below). Consequently, data was modeled using two GLMs: one using the original approach of eliminating Φ_0 by using $\Delta\Phi_m$ and the other using $\Phi_{m,\,TE2}$. The latter assumes Φ_0 to be stable across scans, and thus implicitly incorporates Φ_0 into the GLM intercept.

The remaining terms in equation 11 were modeled as follows: Φ_{Motion} was modeled by including 6 covariates corresponding to the 6 motion parameters (calculated during the realignment step). A similar linear modeling of motion could not be performed in the earlier implementation due to limited degrees of freedom (N=13 vs. 540 here), and arguably would not

be accurate (since one brain volume was acquired every 2.5 minutes). Φ_{Scan}, i.e. phase offsets across MRI scans, were modeled using binary covariates: for instance, a covariate that is '1' for volumes acquired during scan#1 and '0' otherwise, models out any phase offset from scan#1. Because there are a total of three scans, two such covariates and the intercept are sufficient to model Φ_{Scan}, and were included in the GLM.

For both the GLMs described above, the regression coefficients of the applied current predictor can be interpreted as the phase induced per mA applied current. These were scaled using equation 4 to calculate the induced magnetic fields (along B_z) per mA tDCS. This is the same approach as the one used previously (Ch-1, 1.4.1.2). Sensitivity of the two GLMs was calculated to be (a) 0.38 nT, for the GLM based on $\Delta\Phi_m$ (i.e. the original approach) and (b) 0.22 nT, for the GLM based on $\Phi_{m, TE2}$. The calculations utilized equation 6, with ΔTE = 15 msec for (a), and replacing ΔTE by TE_2 (= 26 msec) for (b).

2.4.1.3 Statistical Analysis

Obtained current induced magnetic field maps were subsequently thresholded at $p < 0.05$ and cluster corrected at $p < 0.05$(using AlphaSim(76)) following standard statistical procedures for fMRI. Statistical techniques used to compare experimental results with simulations are described after the 'Simulations' section.

2.4.2 Simulations

Experimental measurements of the tDCS current induced magnetic field (along B_z) were compared with predictions from computational models of tDCS current flow. These models were

constructed by segmenting a structural image of the head, creating a finite element model (FEM) of each tissue and solving Laplace's equation with boundary conditions specified by the tDCS montage. SIMNIBS(86) (v2.0.1, open source) was used to create and solve the FEMs to generate a current-density map. This map was subsequently used to calculate the current induced magnetic fields using the Biot-Savart Law; the latter implemented as a 3D convolution(81).

SIMNIBS constructs a 5-compartment model of the head (GM, WM, CSF, bone and scalp). Unless otherwise specified, isotropic tissue conductivities reported in literature(87) were used. The magnetic permeability of water was used in the Biot-Savart law, since permeability varies on the order of ppm across tissues(69). For all models, a tDCS current of 1mA was used, enabling the simulated fields to be directly compared with the experimental measurements (the latter being the magnetic fields induced per 1 mA tDCS current).

2.4.2.1 Modeling individual subjects (to compare with measurements)

Separate models were constructed for each individual subject to take into account individual head anatomy. Structural data (acquired using a MPRAGE scan) was segmented using SIMNIBS, following which a finite element model was built. Electrodes were positioned using the gel (visible on the structural scan) as a guide. The rest of the modeling steps were the same as described in the section above.

2.4.2.2 Modeling standard MNI head (to explore sensitivity to model parameters)

A tDCS simulation depends on the following model parameters:

1. Electrode Orientation

2. Electrode Shape
3. Electrode Size
4. Electrode Position
5. Tissue conductivity
6. Tissue compartments/segmentation

Except 6, all of the above parameters were perturbed in a standard MNI head to investigate sensitivity of simulations to model parameters.

The possibility of detection in bilateral montages other than the one used in experiments was also investigated. Circular electrodes of 5cm diameter were used, and bilateral montages consisting of anode at one of {F2, F4, F8, C4, T4, P4, T6, O2}, and cathode at one of {F1, F3, F7, C3, T3, P3, T5, O1} were simulated in a standard "MNI" head. The average absolute magnetic field for each montage was compared to the same simulated for the experimental montage (i.e. C3-C4). Additionally, sign-boundaries were extracted from magnetic field maps of {F1} x {All-anode-positions} to map how they changed across montages. Sign boundary extraction was performed using the "Canny" edge extraction method implemented in MATLAB.

2.4.3 Comparing measurements with simulations

SPM8 was used to coregister experimental measurements to the structural MPRAGE. With measurements now present in the same coordinate space as simulations, voxelwise comparisons were carried out as described below.

2.4.3.1 An unambiguous classification scheme to visualize differences

Both measurements and simulations, estimate the tDCS current induced magnetic field (along B_z) in a voxel, which is a signed real number. The signs of the estimates make comparison using a simple difference ("Exp – Sim") ambiguous to interpret. Fig.2 shows a classification scheme devised to unambiguously visualize differences between simulations and measurements. This classification scheme was applied on simple difference maps ("Exp – Sim") of each subject.

A classification scheme to unambiguously visualize differences between Experiments and Simulations

Classification Scheme			An example			
Sign(Exp) ? Sign(Sim)	|Exp| ? |Sim|	Class ID	Exp	Sim	Simple Difference (Exp –Sim)	Class ID
=	>	+4	+4	+2	> 0	+4
	=	+3	+4	–2	> 0 *	–4
	<	+2	–2	–6	> 0	–2
≠	>	–2	As shown by *, the "Simple difference" cannot be used to infer the relationship between Exp and Sim (>,=,<). In contrast, the proposed ID system is unambiguous.			
	=	–3				
	<	–4				

Figure 2. A Classification scheme to unambiguously visualize differences between experiments (Exp) and simulations (Sim): As shown in the example, voxel values in a simple difference map cannot be used to directly interpret the relationship between Exp and Sim. This problem is a result of the fact that the measured magnetic fields possess both magnitude and sign.

2.4.3.2 Insights from a simplified model of current flow

Fig. 3 shows a simplified model of current-flow for the tDCS montage used in experiments. Electric current is assumed to flow into the sagittal plane, which is a good approximation given the bilaterally symmetric montage. Two additional simplifications are assumed: About a point "P" (hereon referred to as the center-of-current), local current density is uniform, and has cylindrical symmetry. With these simplifications, Ampere's law can be used to calculate a closed form expression for the local magnetic fields induced by tDCS currents, as shown in the Fig 3.

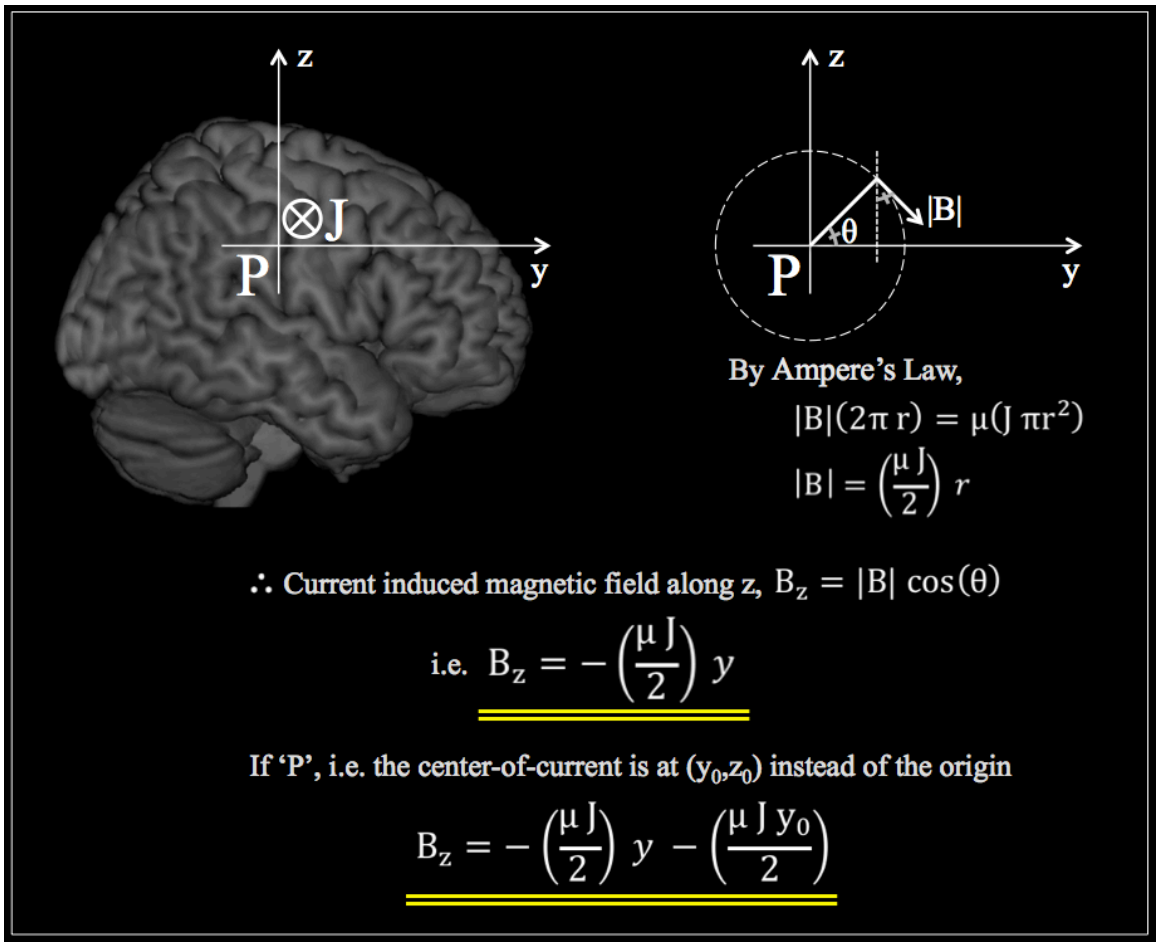

Figure 3. A simplified model of current flow in the C4-C3 montage: Current is assumed to be uniform, and cylindrically symmetric in a local region about a point 'P' (referred to as the center-of-current). With these assumptions, a closed form expression for the current induced magnetic field can be calculated as shown in the figure.

Suppose a current density "J_s" is predicted by simulations. Without loss of generality, the center-of-J_s-current can be chosen as the origin. As a result, the first expression of Fig. 3 can be used to evaluate the magnetic field induced by J_s (henceforth referred to as "B_s"). In general, the actual center-of-current may not match the center predicted by simulations, and thus the second expression of Fig. 3 should be used to evaluate "B_a" (i.e. the magnetic field induced by the 'actual' current density, J_a). The difference (B_a–B_s) was calculated for different cases of {J_a , J_s}, and categorized using the classification scheme described above. The categories observed

provided insights into how characteristic differences in magnetic fields can result from differences between simulated and actual current density.

2.4.3.3 Evaluating the overall significance of differences

The results will show that experimental measurements are systematically different from simulations of the tDCS current induced magnetic field (along B_z) in individual subjects. The results will also show that tuning model parameters in individual subjects (within reasonable limits) can, in principle, mitigate some of these differences. However, are differences between measurements and simulations significant? Or are simulations, based on contemporary modeling approaches, sufficient to model individual subjects?

This question was investigated by evaluating the inter-subject variability of simulated magnetic fields (=σ_s). Intuitively, if this number is less than the actual inter-subject variability (=σ_a), then it follows that simulations do not model individual subjects precisely. Crucially, the magnitude of the difference ($\{\sigma_a - \sigma_s\}/\sigma_s$) can be used to assess if simulations model individual subjects sufficiently. The exact procedure for the calculation of σ_s and σ_a, and the statistical techniques employed are described below.

For each subject, measurements and simulations were normalized to the MNI space using SPM8. Among these, the simulated current induced magnetic field (=β_s) is fully specified by the computational model employed, and is thus deterministic. In contrast, the measured current induced magnetic field is a random variable; and because it is estimated from a GLM, follows a known normal distribution $\mathcal{N}_{i,v}(\beta, \sigma)$. Here, σ represents the measurement-noise at a voxel 'v' in

subject 'i'. As a result, although σ_s can be calculated as the standard deviation (over all subjects) of β_s, the same approach cannot be used to estimate σ_a. This is because the estimate β includes measurement-noise, and thus the standard deviation of β is a combination of σ_a and that measurement-noise.

Measurement-noise corrected estimates of σ_a–σ_s were calculated using a Monte Carlo approach. The measurement noise 'σ', implicitly present in experimental measurements, was introduced into simulation estimates (as shown in equation 12). Repeated randomized sampling was performed to compute a distribution of σ_a–σ_s. This distribution was then used to calculate (a) the probability that the actual inter-subject variability is greater than that predicted by simulations (i.e. $E(\sigma_a - \sigma_s > 0)$) and (b) the average size of the difference, in units of σ_s (i.e. E($\{\sigma_a$–$\sigma_s\}/\sigma_s$)). The denominator σ_s was calculated as described in the previous paragraph.

$$(\sigma_a - \sigma_s)_v[k] = \underbrace{std\left(\mathcal{N}_{i,v}(\beta, \sigma)\right)}_{\sim\ \sigma_a+\sigma} - \underbrace{std\left(\mathcal{N}_{i,v}(\beta_s, \sigma)\right)}_{\sim\ \sigma_s+\sigma} \tag{12}$$

Here, k is the index to one Monte-Carlo estimate of σ_a–σ_s. A total of 10^5 such estimates were computed for each voxel 'v' in the brain. *std*(.) is the standard deviation of (.), calculated over all 'i' subjects.

3. Results

3.1 Experimental measurements

Fig. 4A shows the tDCS setup used in experiments. The tDCS current induced magnetic fields (along B_z) can be intuited using Fleming's right hand rule. As shown in the sagittal slice,

the rule predicts the induced field to be along-B_z in the posterior half of the brain, and opposite B_z in the anterior half. As shown in Fig. 4B, measurements of the induced field matched these expectations. It should be noted that unlike "#1", we were able to measure tDCS induced magnetic fields in individual subjects using the new "#2" implementation (data is shown from three representative subjects in Fig. 4B, using TE_2 data, thresholded at $p < 0.05$, Cluster corrected $\alpha < 0.05$).

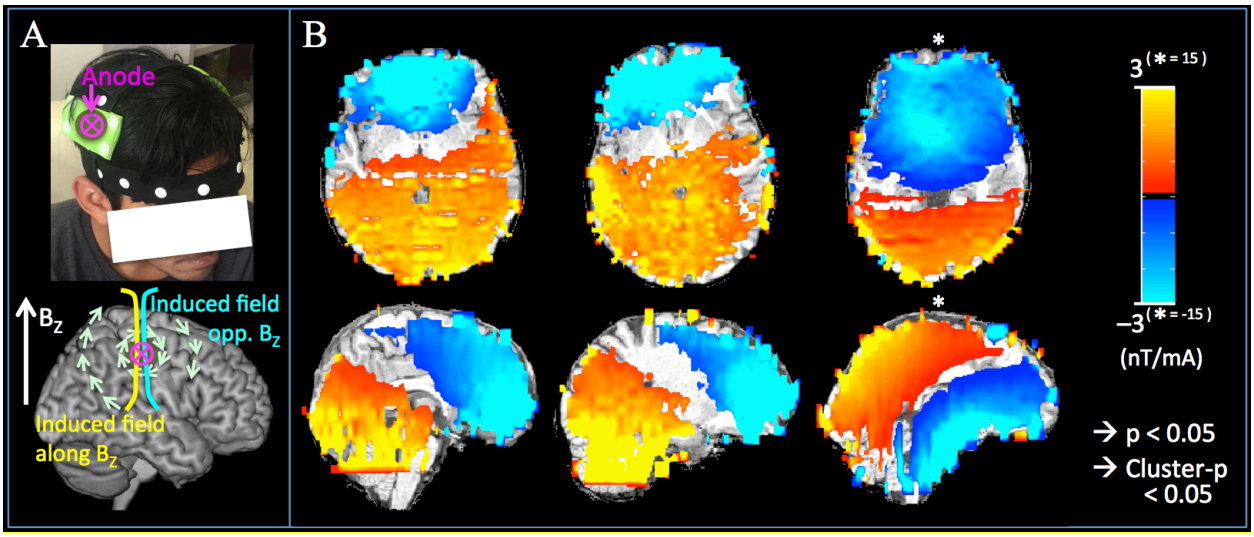

Figure 4. tDCS current induced magnetic fields (along B_z) measured using the "#2" implementation: 4A shows the tDCS setup, and the magnetic fields expected from Fleming's right hand rule. Measured fields matched expectations, as shown by the measurements from three representative subjects in 4B (thresholded to $p < 0.05$, $\alpha < 0.05$ (cluster corrected)).

Comparison between the TE_2 and ΔTE models

The tDCS current induced magnetic fields (along B_z) were estimated using two different GLM's – (a) the original GLM approach, which utilizes the difference of the phase data measured at two TE's, and (b) the improved GLM, which utilizes phase data measured at the second TE. The results generated by both GLM's were very similar (Average correlation across subjects, Pearson = 0.83 ± 0.05; Spearman = 0.89 ± 0.02; $p < 0.001$ for all subjects). Since the

latter GLM (i.e. '(b)') has better sensitivity and noise-characteristics (as shown in 2.4.1.2), all subsequent analysis utilized results from '(b)'.

3.2 Comparing measurements with simulations

Fig. 5 shows the experimentally measured tDCS current induced magnetic fields (along B_z) in column 1, and its simulated counterpart in column 2. Although the experimental measurements qualitatively matched simulations (Average correlation across subjects, Pearson = 0.27 ± 0.08; Spearman = 0.48 ± 0.13; $p < 0.001$ for all subjects), distinct differences between the two were observed. Fig. 5 column 3 shows the difference map ("Exp – Sim") for each subject, and column 4 shows the differences classified according to the scheme described in 2.4.3.1. With the exception of Subject 7, the differences between measurements and simulations were observed to be consistent across subjects, with the measured fields being more negative in the anterior half of the brain, and more positive in the posterior half.

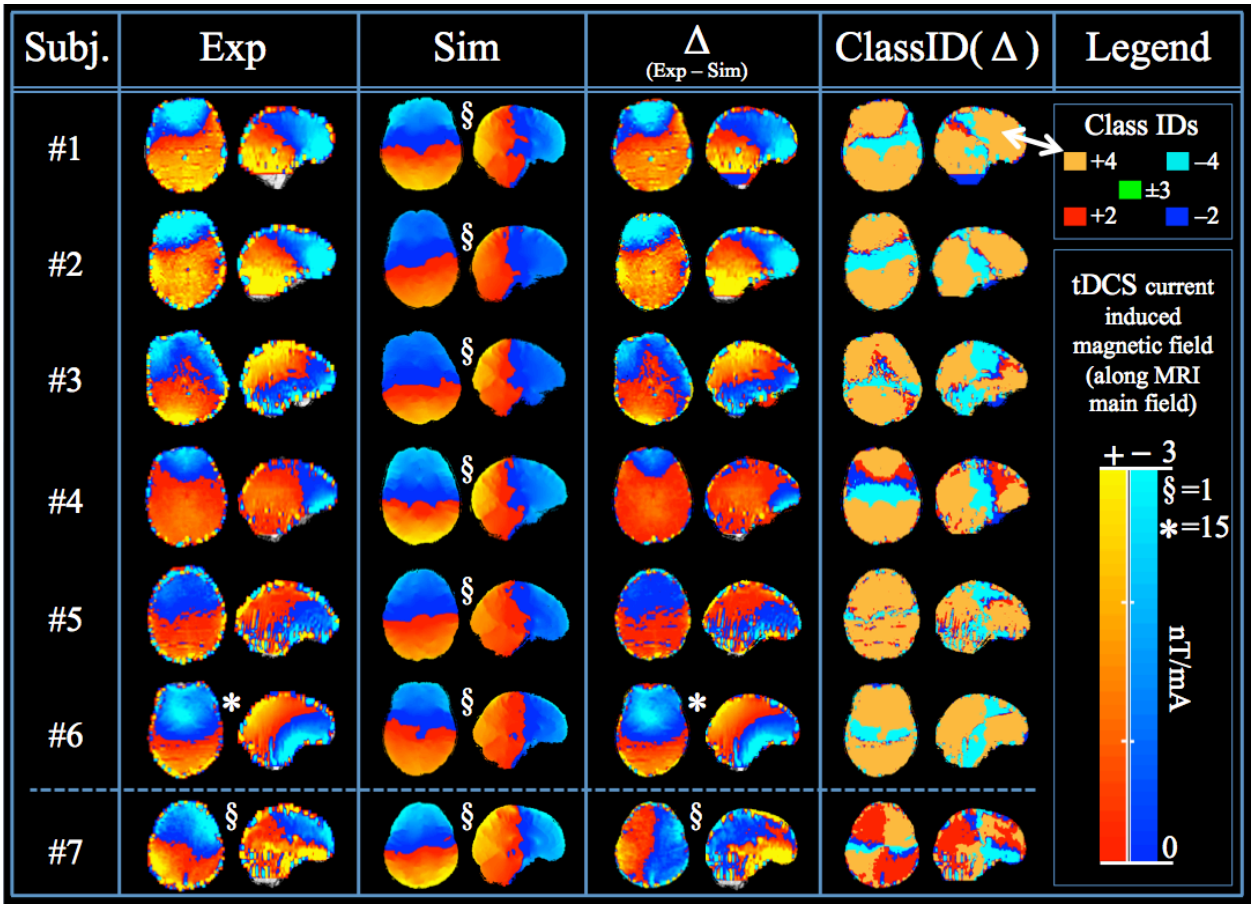

Figure 5. Comparison of measurements with simulations: Column 1 shows the experimental measurements with the simulation results shown in 2. Column 3 shows the difference map, and 4 shows the differences classified according to the classification scheme of Fig. 2. To note is the prevalence of class "+4". "+4" indicates that Exp and Sim are of the same sign, and Exp > Sim. These qualitative observations are quantified in Table 1.

Table 1 summarizes these observed differences. Excluding Subject 7, the experimental measurements were significantly ($p < 0.05$) different from simulations in ~43% of total voxels on average ({min,max} ~ {19,67}%). In the same group, the magnitude of measured fields was greater than simulations in ~88% of the total voxels ({min,max} ~ {86,97}%), with a mean absolute difference of 2.95 nT/mA ({min,max} ~ {0.94,7.39} nT/mA). Moreover, the absolute "Exp – Sim" differences were observed to increase with distance from the sign-boundary (i.e. red-blue boundary in Fig. 5, column 3). An additional difference in the form of oblique sign-boundaries was observed. As can be seen in the sagittal view of Fig. 5 column 3, the sign-

boundaries were measured to be at an angle of ~30^0-45^0 to the Superior-Inferior (S-I) direction, in contrast to simulations which predict an angle of ~0^0.

Subject#	% Voxels		$\overline{\lvert Exp - Sim \rvert}$
	Exp – Sim ≠ 0 ($p < 0.05$)	|Exp| > |Sim|	(nT/mA)
1	50.2	88.3	1.93
2	43.2	92.1	2.97
3	49.9	89.9	2.85
4	26.8	74.0	0.941
5	19.3	86.0	1.62
6	66.8	97.3	7.39
Mean	42.7	87.9	2.95
7	19.2	55.2	0.703

Table 1. Whole-brain measure of the differences between experimental measurements (Exp) and simulations (Sim) in each subject: Excluding subject 7 that appears to be an outlier (as apparent from the difference maps of Fig .5), measurements were significantly larger than simulations in 42.7% of voxels overall, where the significance level was set to $p < 0.05$. Unthresholded, this went up to 87.9% of voxels in the brain, on average across subjects. The average strength of the magnetic field difference was ~2.95 nT.

In Subject 7, although the magnitude of measured fields were greater than simulations in only ~55% of the total voxels, the differences were not random and had spatial structure. These differences were suggestive of a volumetric current component running in the P-to-A direction (discussed below in 4.2), and as a result, models with perturbed electrode positions and conductivities were simulated. As shown in Table 2, the perturbed models improved the match between measurements and simulations. Additionally, as shown by the class ID maps, while the first perturbation made the simulated fields stronger than experiments across the brain, the second made the fields weaker. In both perturbations, the fields had the same sign as experiments. This suggests that parameter values maximizing the match between simulations and measurements exist as a local optimum, bounded by the perturbed values shown.

Comparison of simulations with measurement (Subject #7)

Simulation details		Δ = Exp – Sim	ClassID(Δ)	Observations	Spearman Correlation (Exp, Sim)
		± 0 nT/mA 1	+4 −4 +2 −2		ŦpValue < 0.001
Standard (Same as Fig. 5, #7)				Since MR static field is out-of-the-plane and anode is on RHS ; ← maps suggest a volumetric current in the P-to-A direction. Accordingly, simulation parameters were perturbed	0.32Ŧ
Perturbations					
Electrodes Anode, 1 cm Post. Cathode, 2cm Ant.	+ Conductivity Scalp = 1/14x* GM/WM = 2.5x**			+4 classID → Exp > Sim && Sign(Exp) = Sign(Sim)	0.47Ŧ
	+ Conductivity GM/WM = 1/2.5x**			+2 classID → Exp < Sim && Sign(Exp) = Sign(Sim)	0.44Ŧ
				These suggest that a conductivity value s.t. Exp ≈ Sim exists	

* Björklund S., et. al., Biophys J. 2013 Jun 18;104(12):2639-50. ** Akhtari M., et. al., Brain Topogr. 2010 Sep;23(3):292-300. Epub 2010 May 4.

Table 2. Measurement-suggested perturbations of simulations in Subject 7: The differences between experiments (Exp) and simulations (Sim) in subject 7 suggested perturbations in the model parameters. Parameters were perturbed within reasonable limits (considering that the electrode length in the A-P direction was 9cm, and using conductivity values reported in literature (88, 89)). While the first perturbation made the simulated fields stronger than experiments across the brain, the second made the fields weaker. In both perturbations, the simulated fields had the same sign as experiments for the most part (as indicated by the class ID maps).

3.2.1 Insights from a simplified model of current flow

The previous section compared experimental measurements of the tDCS current induced magnetic field (along B_z) with simulations. With the exception of subject 7, the following differences were observed: (a) The magnitude of measurements was consistently larger than simulations, (b) the absolute "Exp-Sim" differences increased with distance from the sign boundary, and (c) the sign-boundaries in the sagittal plane were at an angle of ~30^0-45^0 to the S-I direction. In this section, we show how (a) and (b) can potentially result from differences in current densities using a simplified model of current flow.

In the model described in 2.4.3.2 (summed up in Fig. 6), the current induced magnetic fields are linear functions of 'y', where y is the Anterior-Posterior direction (y+ = Anterior). In particular, the 'simulated' magnetic field in the z-direction ($B_{z,s}$) is a linear function of 'y' with a

slope proportional to the current density predicted by simulations (J_s) and zero intercept. Similarly, the 'actual' magnetic field ($B_{z,a}$) has a slope proportional to the actual current density (J_a) and an intercept ('c'); the latter depending on the position of the actual center-of-current.

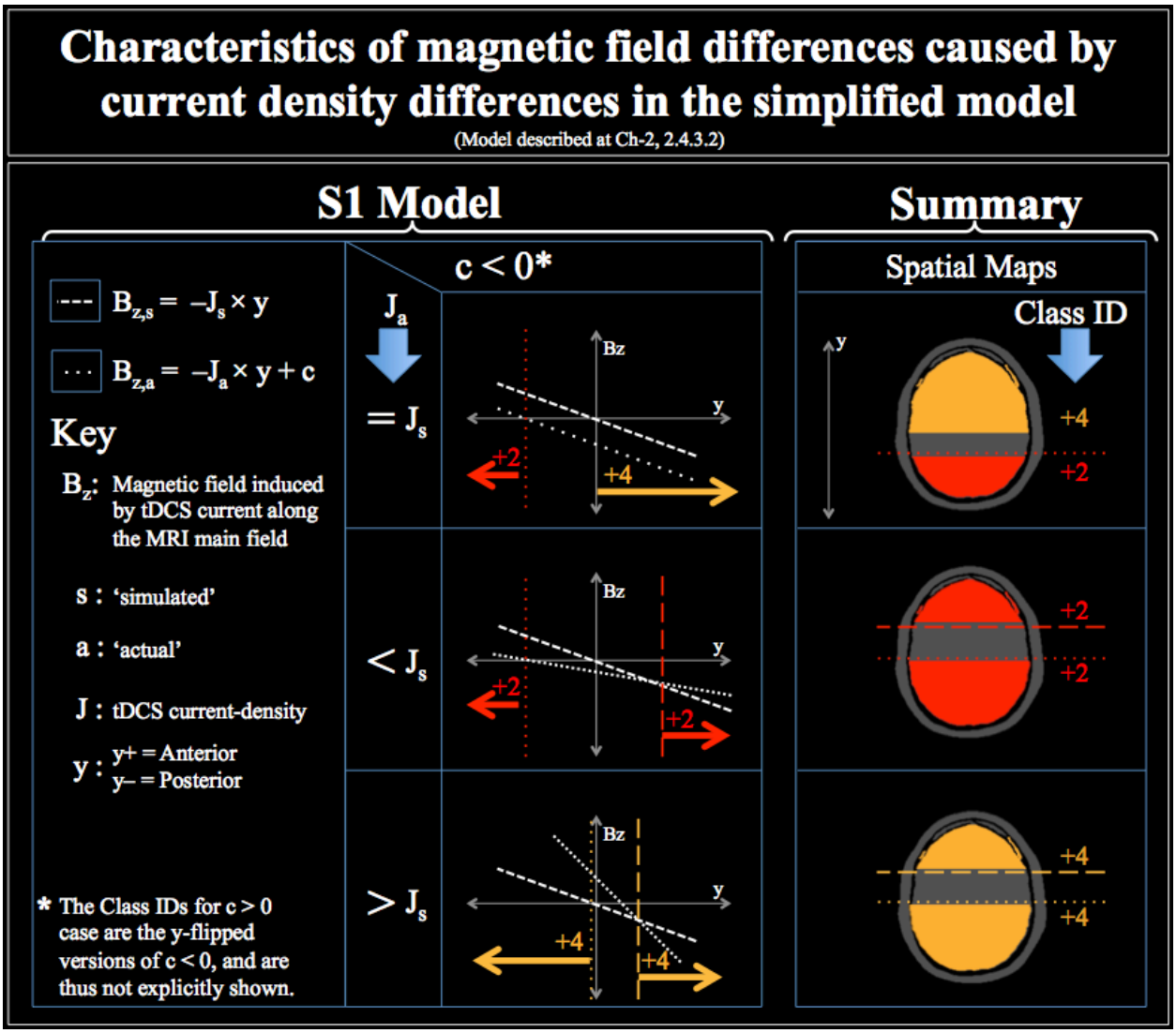

Figure 6. Insights from a simplified model of current flow (described in Ch-2, 2.4.3.2): Different cases of the relationship between the 'actual' current density (J_a) and that predicted by simulations (J_s) generate characteristically different induced magnetic fields. In particular, for $J_a > J_s$ (last row), the model predicts (a) the magnitude of the actual field to be stronger than the simulated field, (b) the magnetic field difference to scale linearly with the distance in the A-P direction, and (c) the class ID maps to be dominated with "+4" in the A/P regions. The latter occurs only when $J_a > J_s$.

Each plot in Fig. 6 graphs the 'simulated' and 'actual' magnetic fields (induced by their respective current densities). Rows 1,2,3 show the cases of the actual current density 'J_a' being {=, <, >} than the simulated current density 'J_s'. Only results for 'c < 0' are shown since the class ID's for 'c > 0' are essentially the same as 'c < 0' flipped about the origin. As summarized in the table, the majority of voxels fall into distinct classes for each case. In particular, it should be noted that for $J_a > J_s$, (a) the majority of voxels are of class +4 (brown), and (b) the absolute "B_a–B_s" difference increases with distance from the origin. These characteristics are similar to those observed in the comparison of experimental measurements with simulations (Fig. 5).

3.2.2 Sensitivity of simulations to model parameters

Table 3 shows the effect of perturbing various model parameters on the simulated tDCS current-induced magnetic field (along B_z). Perturbations in tissue conductivity cause the mean magnetic fields to change by 0.2nT/mA, and all other perturbations cause changes that are an order of magnitude weaker. Magnetic field maps corresponding to the conductivity perturbations are shown in Table 4, together with maps of a standard simulation for comparison. Additionally, motivated by the oblique sign-boundary observed in measurements, electrodes oriented at 45^0 were simulated. However, orientation of electrodes did not affect the orientation of the sign boundaries (Table 4, 'Orientation' row). However, perturbations in tissue conductivity did affect the sign boundaries (first two rows in Table 4).

Simulation	Description	$\overline{\lvert \text{Perturb.} - \text{Standard} \rvert}$ (nT/mA)
Standard	4.5x9cm electrodes on C4(+)/C3(–) {i.e. Experimental Montage} + Standard simulation parameters	N/A
↓Perturbations↓		
Shape	Circular Electrode (5cm diameter)	0.008
Size (25%)	Electrode dimensions ↑	0.0103
	Electrode dimensions ↓	0.0048
Conductivity	Scalp conductivity = 1/14x*	0.1981
	&& GM/WM = 2.5x**	0.2710
Anode Position (25%)	Anterior (=.25x9cm)	0.0372
	Posterior (=.25x9cm)	0.0361
	Right (=.25x4.5cm)	0.0214
	Left (=.25x4.5cm)	0.0209
Orientation	Ant. end of electrode = $+45^0$	0.0033
	Post. end of electrode = -45^0	0.0031

* Björklund S., et. al., Biophys J. 2013 Jun 18;104(12):2639-50.
** Akhtari M., et. al., Brain Topogr. 2010 Sep;23(3):292-300. Epub 2010 May 4.

Table 3. Effect of perturbing various model parameters on the simulated current induced magnetic field in a C4(+)/C3(-–) tDCS montage in an MNI brain. The effect is calculated as the absolute difference, averaged over the brain. Perturbations in tissue conductivities were observed to cause the largest changes in the induced magnetic field (by an order of magnitude).

Simulation		Magnetic Field Map
Standard	4.5x9cm electrodes on C4(+)/C3(–) {i.e. Experimental Montage} + Standard simulation parameters	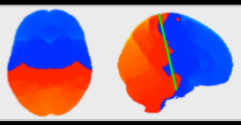
↓Perturbations↓		
Conductivity	GM = 2.5x && WM = (1/2.5)x	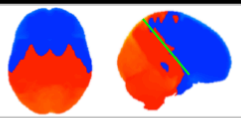
	Scalp conductivity = 1/14x && GM/WM = 2.5x	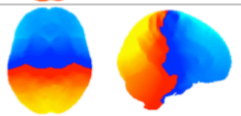
Orientation	Ant. end of electrode = $+45^0$	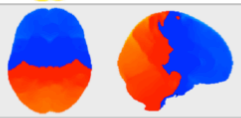
	Ant. end of electrode = -45^0	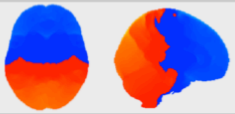

Table 4. Effect of perturbations on the sign boundary: Sign boundaries were observed to change in simulations that used perturbed tissue conductivities. Conductivities were perturbed using values reported in literature(88, 89). Changing electrode orientations by ± 45^0 had comparatively little-to-no effect.

3.2.3 Overall significance of differences

Fig. 7 shows the significance of the differences between measurements and simulations, calculated using Monte-Carlo simulations with the outlier Subject 7 excluded. 7A shows the probability that the measured inter-subject variability (σ_a) of the tDCS current induced magnetic field (along B_z) is greater than its simulated counterpart (σ_s). 87% of the voxels were observed to be above 0.80, and all of the voxels were above 0.50. 7B shows the average size of the difference normalized to σ_s (i.e. $E(\{\sigma_a - \sigma_s\}/\sigma_s)$, with 96% of the voxels in the brain being larger than 3. Similar results were obtained when Subject 7 was included (88% of voxels were above a probability of 0.80, all voxels were above 0.5, and 96% of total voxels had an average difference larger than 3). Note that as described in 2.4.3.3, these measures have been corrected for measurement-noise.

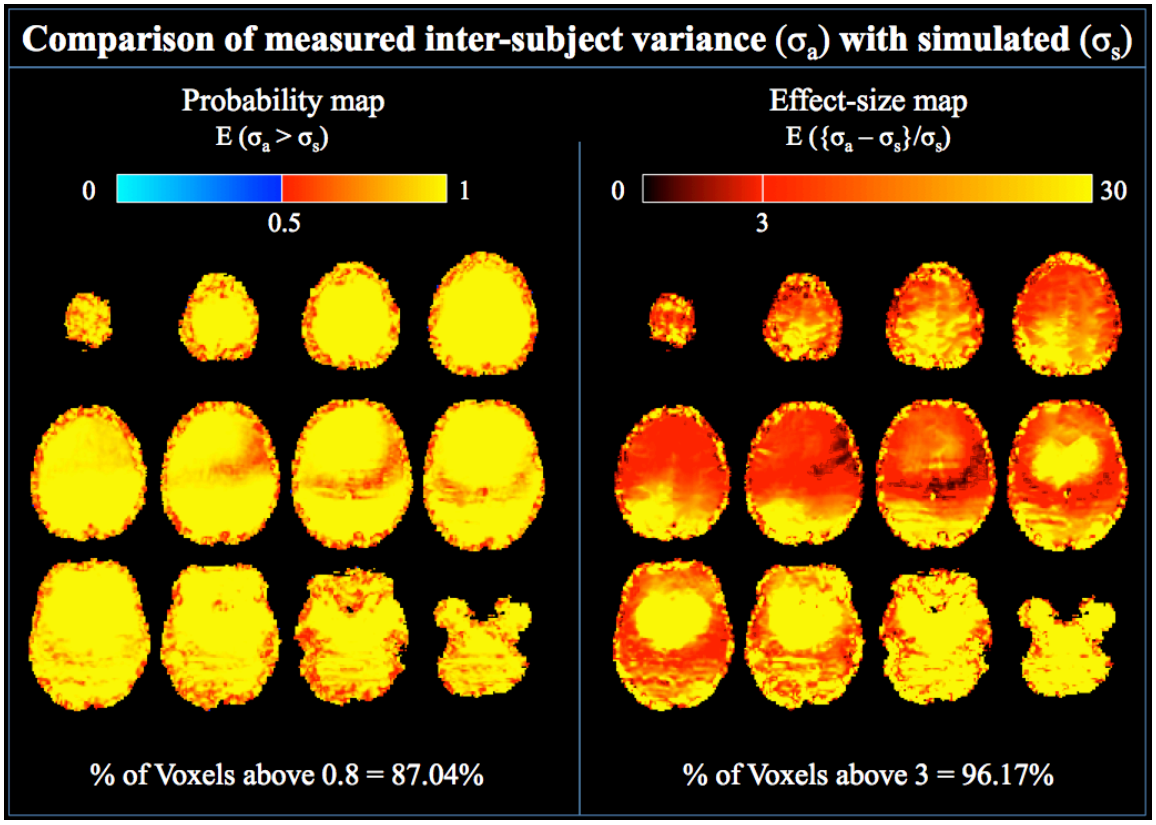

Figure 7. Comparison of inter-subject variability as predicted by measurements and simulations using a Monte-Carlo approach: Results show that the probability of actual inter-subject variability being greater than that predicted by simulations was > 0.8 in 87 % of voxels, and 96% of voxels had an inter subject variability at least three times larger than that predicted by simulations, suggesting simulations are "too similar" across subjects. Note that this calculation took into account measurement noise (as described at 2.4.3.3).

3.3 Simulations of additional bilateral montages

As shown in Fig. 8, simulations predicted the average absolute magnetic fields (along B_z) in most montages to be larger than that in the C3-C4 montage. Of the 36 montages simulated, only 6 showed weaker fields (highlighted in blue), with the smallest field being 50% weaker than that in the C3-C4 montage.

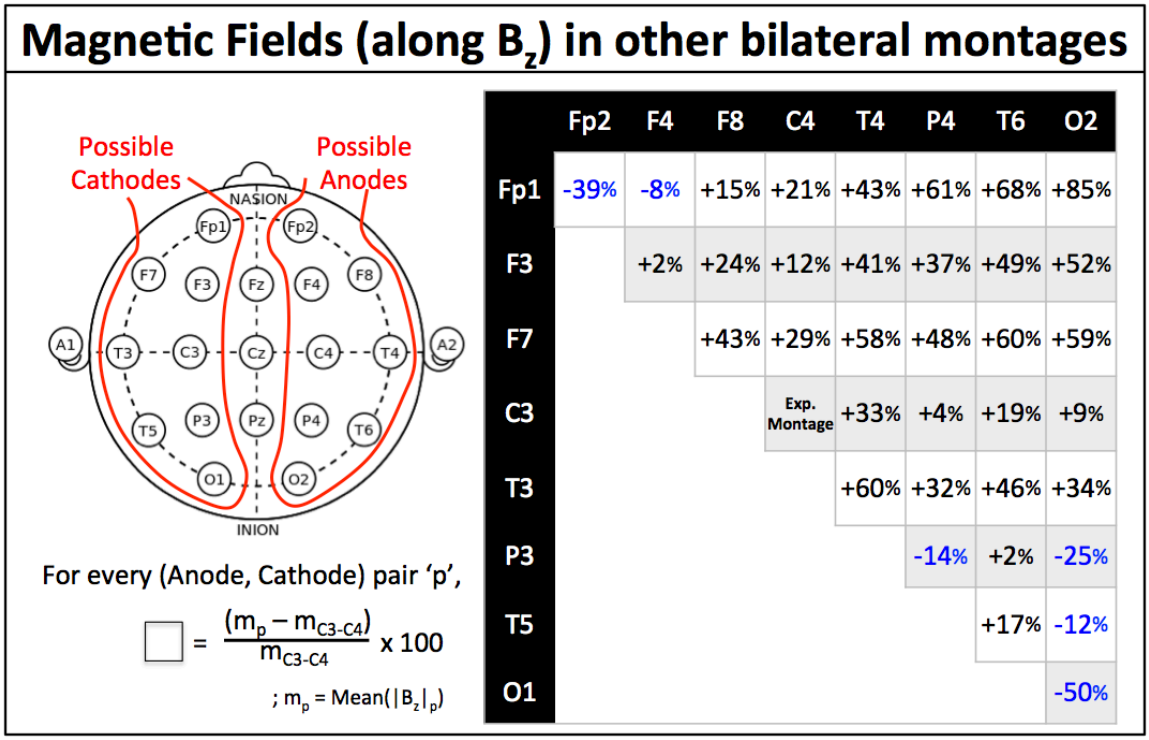

	Fp2	F4	F8	C4	T4	P4	T6	O2
Fp1	-39%	-8%	+15%	+21%	+43%	+61%	+68%	+85%
F3		+2%	+24%	+12%	+41%	+37%	+49%	+52%
F7			+43%	+29%	+58%	+48%	+60%	+59%
C3				Exp. Montage	+33%	+4%	+19%	+9%
T3					+60%	+32%	+46%	+34%
P3						-14%	+2%	-25%
T5							+17%	-12%
O1								-50%

Figure 8. Magnetic fields induced in other bilateral montages, compared to C4-C3 (i.e. experiment montage): 29/35 montages had an average magnetic field greater than C4-C3, suggesting the "#2" implementation could be used for detection in cases other than the experiment montage. However, montages with fields smaller than C4-C3 were also observed (highlighted in blue), with the smallest field being 50% weaker than that of C4-C3.

Fig. 9A shows the spatial distribution of the simulated current induced magnetic fields for the following montages: Cathode(F1) x Anode(F2, F4, F8, C4, T4, P4, T6, O2). Sign boundaries from each of these simulations were extracted and were observed to (i) change across montages, and (ii) lie along sulci in the fronto-parietal cortex (Fig. 9B).

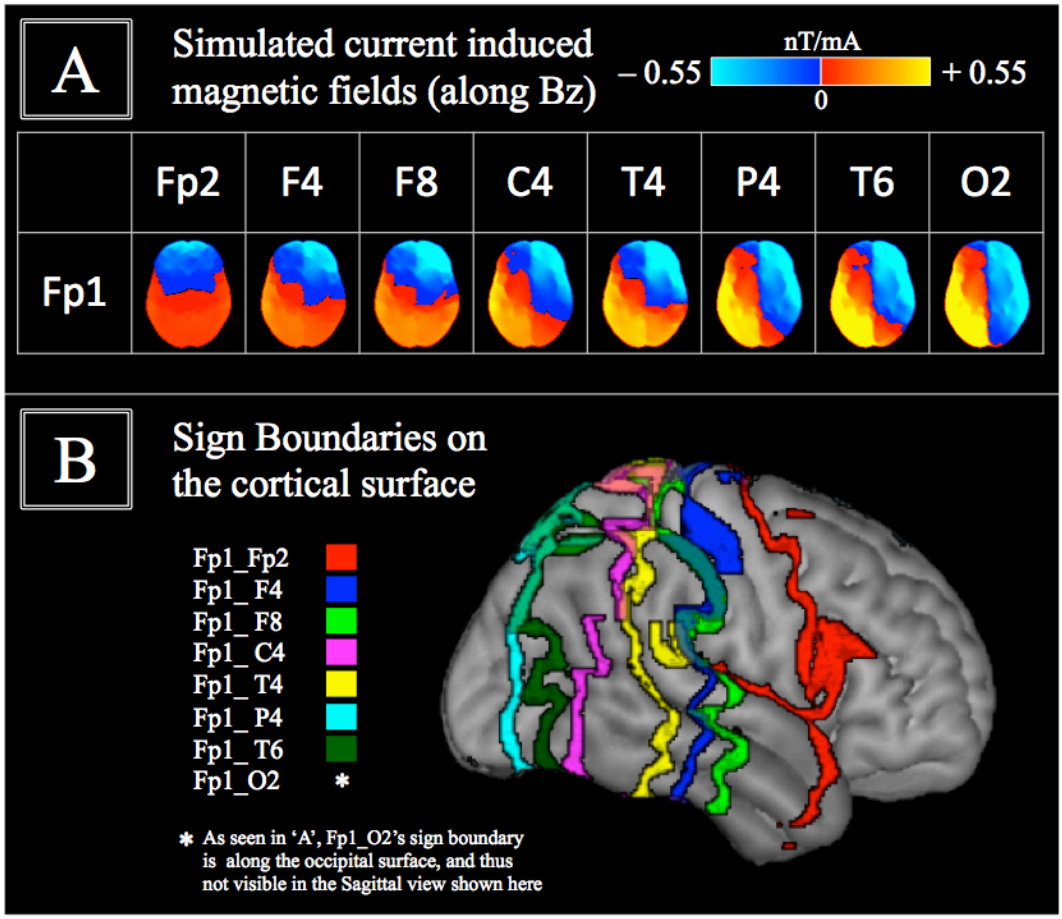

Figure 9. Changes in the sign boundary with montages: Simulations show that besides changes in the strength of the magnetic field with montages (A), the sign boundary surface also shifts distinctly (as shown in B), suggesting that this surface could be a useful feature in tracking montages, and possibly targeting.

4. Discussion

4.1 Validity of the "#2" implementation

The "#2" implementation was developed to detect the tDCS current induced magnetic fields (along B_z) in individual subjects. To demonstrate this capability, seven healthy subjects were recruited and concurrent tDCS-MRI experiments were performed using a bilateral montage targeting the motor cortices (anode/cathode = C4/C3). Qualitatively, the fields measured in individual subjects matched expectations from Fleming's right hand rule, which were that the magnetic fields in the anterior half of the brain should be opposite B_z, and the fields in the

posterior half should be along B_z. Additionally, the two GLM approaches used in estimating the induced magnetic fields were in excellent agreement with each other (Average correlation across subjects, Pearson = 0.83 ± 0.05; Spearman = 0.89 ± 0.02; $p < 0.001$ for all subjects) validating the GLM based on TE_2. The GLM based on TE_2 makes assumptions about the baseline phase, but has better sensitivity (0.22 nT vs. 0.38 nT).

4.2 Comparing measurements with simulations

Measurements of the tDCS current induced magnetic fields (along B_z) were compared to simulations. The latter use standard modeling approaches(44, 46, 47, 86) to calculate a current density map as follows: (i) An individualized finite element model (FEM) is constructed using structural MRI data for each subject, (ii) conductivity values for each tissue in the FEM are assigned according to average conductivities reported in literature(87) and (iii) Laplace's equations are solved on the FEM to calculate current density maps. The latter were used with the Biot-Savart law to calculate the induced magnetic fields in each voxel. A significant correlation ($p < 0.001$) between experimental measurements and simulations was observed, with an average correlation of 0.27 ± 0.08 (Pearson) and 0.48 ± 0.13 (Spearman). However, distinct differences between measurements and simulations were observed, as discussed below.

Case of Subject 7

Compared to other subjects, the differences between measurement and simulation in Subject 7 were markedly different. As shown in Fig. 5, the sign boundary of the difference map was observed to be in the A-P direction, with the differences being opposite B_z on the anodal side, and along B_z on the cathodal side. Additionally, the magnitude of the differences was

observed to increase with distance from the sign boundary. These properties, together with the class ID maps and Fleming's right hand rule, are suggestive of a volumetric current running in the P-to-A direction.

A potential cause of this could be the position of the 'effective electrode', where the latter refers to the gel-wetted scalp and the electrode combined. This hypothesis was tested, and perturbations in the electrode position and conductivity were found to improve the match between measurements and simulations (Table 2). The perturbations used are within reasonable limits, considering the 9cm length of the electrode (A-P direction) and variation in conductivities reported in literature(88, 89). Furthermore, the results suggest that parameter values maximizing the match between simulations and measurements exist as a local optimum, bounded by the values tested in Table 2. Such an approach of determining conductivities and 'effective electrode' positions by fitting to measurements could be used to verify targeting in tDCS (discussed below in future developments, 4.4).

Case of all other subjects

The following differences between measurements and simulations were observed consistently across subjects: (a) the magnitude of experimental measurements was consistently larger than simulations (|Exp| > |Sim| in ~88% of total voxels, Table 1), (b) the absolute "Exp – Sim" difference increased with distance from the sign-boundary (Fig. 5, column 3), and (c) the sign-boundaries were at an angle of ~30^0-45^0 to the S-I direction (Sagittal view in Fig. 5).

Of these, we first consider (a) and (b). The spatial and across-subject consistency of (a) and (b) strongly suggest that the source of these differences is systemic, and not stochastic. Besides scaling with distance from the sign boundary (i.e. (b)), the differences additionally scale linearly with the applied current. The latter is a consequence of the fact that (i) the measurements are, by definition of the GLM, magnetic fields per applied current, and (ii) the simulated fields are linear functions of the applied current (because the FEM is a purely resistive network, and the Biot-Savart law is linear).

Could the systemic differences be due to instrumentation/environmental sources (e.g. off-resonance, T2* decay, coils)? Off resonance unrelated to applied current is modeled out as the GLM intercept, and can be ruled out. Off resonance due to the applied current is the signal of interest. T2* decay is not expected to cause changes in the phase signal in image space. Additionally, it is not expected to scale with the applied current since calculations show that T2* decay causes a signal change of ~40% (= 1 – exp(-TE/$T2^*_{GM}$) ; using $T2^*_{GM}$ reported in Kruger et al.(90)). In contrast, current induced magnetic fields cause a signal decay of at most 0.02% (calculation shown in Ch-3, 1.2.1). Coming to the coils, the current induced magnetic fields are static and too small to interfere with the coils inductively. Additionally, interference in coils from tDCS would not explain the observed spatial scaling (i.e. (b)) since within a TR, each k-space line acquired by the coil sees the same DC current. In summary, the two scaling properties together make it unlikely for the primary source of differences to be off-resonance, T2* decay or coils.

A clue in identifying the source of the observed differences is provided by the sign boundary. The sign boundary in the difference maps (axial view) was observed to be ~ in the R-L direction, with the differences being opposite B_z in the anterior region of the brain, and along B_z in the posterior. Additionally, the magnitude of the differences was observed to increase with distance from the sign boundary. These observations, together with the class ID maps and Fleming's right hand rule, are suggestive of a volumetric current component running from the anodal to the cathodal side; indicating a larger current density in the brain than predicted by simulations.

The effect of differences between predicted and actual current densities on magnetic fields was investigated in a simple model. Current flow for the experimental tDCS montage was modeled as a uniform, locally cylindrically symmetric current density. Although this assumption cannot be generalized to the whole brain; locally, it is a reasonable approximation considering the bilateral symmetry of the tDCS montage. This assumption allows an analytical expression to be calculated for the magnetic field induced in a local region. As shown in Fig. 3, the current induced magnetic field is proportional to the applied-current*anterior-position (using the fact that J is directly proportional to the total applied current). Additionally, the model also predicts that among all possible relationships between the 'actual' current density J_a and its simulated counterpart J_s, only $J_a > J_s$ generates differences in magnetic fields that scale linearly with applied current, and possess both (a) and (b) properties (Fig. 6).

Current density being a source of the observed differences is also suggested by the reports of large variances in tissue conductivities. Although contemporary practice in simulations

is to use average conductivities reported in literature, Björklund S. et al.(89) report the conductivity of the stratum corneum (SC) to vary by as much as 14x depending on hydration. Since the impedance of skin resides mostly in the SC(89), we used the 14x factor to perturb skin conductivity in our simulations. Akhtari et al.(88) report GM+WM tissue conductivity to vary by as much as 243% between subjects. This was the reason a perturbation factor of 2.5x was used for GM/WM conductivities. Simulations showed that perturbations in tissue conductivity cause the largest changes in magnetic fields (by an order of magnitude, Table 3). This suggests that among all other model parameters, tuning tissue conductivities may be key in resolving the observed differences. Note that unlike tissue conductivities, magnetic permeability (the scaling factor that relates current density to induced magnetic fields) varies on the order of ppm across tissues, and can be ruled out as a cause of the observed differences.

Finally, we consider (c), i.e. the oblique sign boundaries. The sign-boundaries are located in regions where the measured magnetic field is the weakest. While a weak signal might suggest random noise to be the source of obliqueness, the spatial smoothness of the sign-boundary indicates that the source is more likely to be systematic. Two systematic causes of an oblique sign boundary are (i) head-position (or more precisely, the angle between the S-I direction and the MRI static field) and/or (ii) an oblique current flow in the head. The angle between the S-I direction and MRI static field was at most 5^0 degrees across subjects (calculated from the qform matrices), which is much lower than the observed 30^0-45^0 angles. We next investigated oblique current flow by simulating electrodes at different angles (no change in sign boundary), and altering tissue conductivity (caused changes in sign boundary, Table 4).

The analyses above demonstrate that across all subjects (except #7), the differences between measurements and simulations are systemic, and are likely due to differences in current densities in the brain rather than measurement related biases. The analyses also demonstrate that these differences can be mitigated in principle by tuning model parameters (e.g. tissue conductivity). Note that these findings are consistent with Chapter 1's results. The only experiment in Ch-1 where measurements matched simulations utilized a phantom constructed such that simulations were purely dependent on geometry, and did not utilize conductivities.

The necessity of tuning model parameters in individual subjects is indicated by the fact that the simulations are "too similar" across subjects (i.e. the inter-subject variability predicted by simulations (σ_s) on average is < 33% of the 'actual' inter-subject variability (σ_a) in 96% of the voxels in the brain). Note that this measure accounts for measurement-noise, as described in 2.4.3.3. The significance of these differences is lower, possibly due to the small number of subjects (Probability ($\sigma_a > \sigma_s$) > 0.8 in 87% of total voxels, and >0.5 in 100% of voxels). Tuning the tissue-conductivity parameter in simulations would be a solid starting point to resolve the observed differences, since the reported variance in conductivities causes large changes in simulations (Table 3), which suggests against using an average conductivity estimate in computational models.

4.3 Advantages of the "#2" implementation

In chapter 1, we saw the advantages of the proposed approach to visualize tDCS currents through a component of its induced magnetic field. Briefly, these were (i) the induced magnetic field is directly induced by, and linearly proportional to the applied current (in contrast to

surrogate markers of current flow), (ii) the physical constant involved in the relationship between direct current and induced magnetic field is highly stable across tissues (varies on the order of ~ppm(69)) (iii) Detection requires no alterations in the applied tDCS current waveform (in contrast to alternative imaging approaches(62, 71, 72)) and (iv) detection employs a GLM approach similar to fMRI, which allows statistical techniques developed for the latter to be adapted for the proposed technique.

The "#2" implementation adds to these advantages by making it possible to perform measurements in individual subjects. While detection in the C4-C3 montage was demonstrated through experiments, simulations in 29 out of 35 bilateral montages showed average magnetic fields to be stronger than those in C4-C3 (Fig. 8). This indicates that the proposed technique should be capable of performing detection in most bilateral montages, and not just the C3-C4 used in experiments. Additionally, the signs of measurements were observed to contain useful information. In particular, the spatial distribution of the sign boundary could potentially be used to track targeting, as suggested by the case of Subject 7 and by Fig. 9 (the latter illustrating how sign boundaries change across some montages).

4.4 Limitations and future developments

The proposed technique measures a single component of the tDCS current induced magnetic field in 'N' voxels. In the absence of additional information, mapping electric current requires measuring all three spatial components of the induced field, or '3N' measurements. However, if the head geometry is known, the number of unknowns in a typical simulation (e.g. montage specifics, tissue conductivities) are unrelated to 'N'. This suggests that it could be

possible to use the relatively large number of 'N' measurements to tune model parameters and obtain accurate simulations of current flow in tDCS. The caveat to this approach would be montages that generate weak fields along the measured component i.e. have the majority of current flow in the S-I direction. However, since most montages have some current flow in directions other than S-I, detection should be feasible given adequate sensitivity.

The limitations of the present implementation are the sensitivity and reliability of measurements. Although detection in the majority of bilateral montages appears feasible, simulations predict weaker magnetic fields in a small number of montages (Fig. 8, in blue). Thus, the "#2" implementation needs further improvements before it can become a general-purpose detection technique for tDCS. Future developments will investigate increasing the TE (to improve sensitivity), and reducing TR (from 4 seconds to 2). The latter will result in an increase in the number of measurements and thus, improve the reliability of magnetic field estimates.

A promising direction for research involves integrating fMRI with our magnetic field mapping technique. While our technique uses the phase information in an MRI image, most existing fMRI methods use magnitude. Since every MRI acquisition generates phase and magnitude images, it is conceivable that target engagement (through mapping tDCS induced magnetic fields) and ensuing neurophysiological effects (through BOLD/ASL fMRI) could be simultaneously measured during a single tDCS session. One such promising technique is ASL with dual-echo EPI readout(91) to simultaneously map current induced fields, perfusion and blood oxygenation.

5. Conclusion

This chapter discusses the development of the state of the art implementation that was used to detect tDCS current induced magnetic fields in individual subjects. Next, the measurements were compared to simulations revealing systemic differences between the two. Analysis suggested that these differences were potentially due to current density differences between measurements and simulations. Finally, these differences could be mitigated to an extent by tuning simulation parameters in individual subjects.

Chapter 3: Concurrent measurement of neurophysiological changes induced by tDCS

1. Theory

1.1 Components of the MR signal: 'magnitude' and 'phase'

Physically, the MR signal measures the spin of hydrogen nuclei in a plane perpendicular to the MRI static field. Because the measured signal lies in a plane, it is a two-dimensional vector, and is represented in the acquired data as the length of the vector (or 'magnitude'), and the angle of the vector to a reference (or 'phase'). As the names suggest, the 'magnitude' is sensitive to processes that alter spin-strengths (e.g. T1/T2/T2* decay), and the 'phase' angle is determined by factors that affect the spin rotational rate. The latter is directly proportional to the local magnetic field, according to the Larmor equation:

$$\omega = \gamma \times B \tag{13}$$

where ω is the spin rotational rate, γ is the gyromagnetic ratio for protons and B is the local magnetic field.

The proposed approach to visualize tDCS currents is based on Ampere's law, which states that an applied current induces a magnetic field. These induced fields affect the average magnetic field in a voxel, which in turn affects the spin rotational rate, and consequently the 'phase' of the MR signal. Changes in the 'phase' signal due to tDCS currents were successfully detected in individual subjects using the "#2" implementation.

In contrast to 'phase', the 'magnitude' signal remains unused in the "#2" implementation (only used in SNR thresholding). The magnitude signal has the same properties as the phase signal (i.e. identical size and spatiotemporal resolution) and is acquired at no extra cost. Consequently, the feasibility of utilizing the magnitude signal was investigated. Specifically, I focused on using the magnitude signal to measure neurophysiological changes, to develop a capability to concurrently map (i) the tDCS-intervention (through current induced magnetic fields) and (ii) the ensuing brain-response. Once developed, this capability should open a new avenue to investigate the mechanisms of tDCS, and improve its therapeutic potential. This was the final aim of my PhD research.

1.2 The "#2" implementation revisited: Encoding neurophysiological changes as BOLD-contrast in the unused 'magnitude'

The feasibility of measuring tDCS-induced neurophysiological changes was investigated using the Blood Oxygenation Level Dependent (BOLD) contrast. The BOLD contrast was chosen because (i) BOLD is an established marker for neuronal activity(50-52), and (ii) the standard BOLD MRI sequence is similar to the sequence used in the "#2" implementation. Because of the latter, only the echo time of the "#2" implementation needs to be adjusted to acquire BOLD contrast in the magnitude signal. This was partly the reason for choosing the second echo (TE_2) of the "#2" implementation in Chapter 2 as 26 msec (the other reason being the improved sensitivity and reduced noise of magnetic field measurements, as described in Ch-2, 2.1.2).

1.2.1 Interactions between BOLD and tDCS current induced magnetic fields

The BOLD contrast in MRI is generated by the hemodynamic response to local neuronal activity changes(50-52). The hemodynamic response causes fluctuations in the concentration of deoxyhemoglobin. Because the deoxyhemoglobin molecule is paramagnetic, it perturbs the local magnetic field and causes each nearby spin to gain a slightly different phase. The increase (/decrease) in the variance of phase due to an increase (/decrease) in deoxyhemoglobin causes an overall drop (/increase) in the magnitude signal, recorded as the BOLD signal. The increase (/decrease) in phase variance however, is not expected to perturb the mean phase in a voxel and consequently, the BOLD signal is not expected to affect the voxelwise magnetic field measurements.

Next, we evaluate the possibility of tDCS induced magnetic fields affecting the BOLD signal. Consider a cubic voxel having a magnetic field ranging from 0 to ΔB_z between two opposing faces. Such a magnetic field would induce spin-phases ranging from 0 to Θ radians. Assuming that ΔB_z is spread linearly over the voxel, the % change in magnitude due to this magnetic field disturbance can be calculated as:

$$\%\ change\ in\ magnitude = \left(1 - \frac{2\ sin(\Theta/2)}{\Theta}\right) \times 100 \qquad (14)$$

The strongest magnetic fields measured in experiments ranged from -15 to 15 nT over ~100 voxels in the brain. Even assuming a ~10nT magnetic field disturbance over 1 voxel, the resulting % change in the magnitude signal is ~0.02% (Θ calculated using ΔB_z = 10 nT, TE of the "#2" implementation i.e. 26 msec, and equation 4). A typical BOLD signal change is one to two orders of magnitude larger, and consequently tDCS current induced magnetic fields are not expected to affect the BOLD signal.

2. Methods

2.1 Experiments

To provide a proof of concept that tDCS current induced magnetic fields (along B_z) and ensuing neurophysiological changes can be measured simultaneously, magnitude data from the dataset of Chapter 2 was used for analysis. While the phase of this dataset has been used to estimate the induced fields, the magnitude signal at the second echo contains the BOLD contrast (as discussed in the previous section). Full details of the experimental design and setup are described in Chapter 2. In brief, tDCS was delivered using a bilateral montage targeting the motor cortices, and subjects were asked to fixate on a resting state cross (white on black background) during the scan.

2.2 Data Analysis

BOLD-contrast data from the three scans was concatenated and corrected for motion by realigning all volumes to the first (using SPM8). Data was then smoothed using an 8 mm isotropic gaussian kernel, and corrected for drifts using quadratic polynomial detrending. Next, the data was modeled voxelwise using a General Linear Model (GLM) with the applied current as a predictor and motion parameters as nuisance covariates. The predictor parameter estimate can be interpreted as the %BOLD change per mA tDCS.

The predictor parameter estimate maps from each subject were coregistered to their corresponding structural images and subsequently normalized to the MNI space. The normalized

maps were used to perform a group level analysis (1 sample t-test) to identify regions of the brain that respond consistently to tDCS stimulation. Because of the GLM, these regions can be interpreted as showing a linear dose response to tDCS across subjects.

3. Results

As shown in Fig. 1, a significant linear dose response of the BOLD signal to the applied tDCS was observed at {L. M1, Insula, ACC, R. Caudate, and L. parietal/occipital lobe}. The significance threshold was set to $p < 0.05$, with cluster size > 100. A decreased BOLD response was also observed near the R. ventricle.

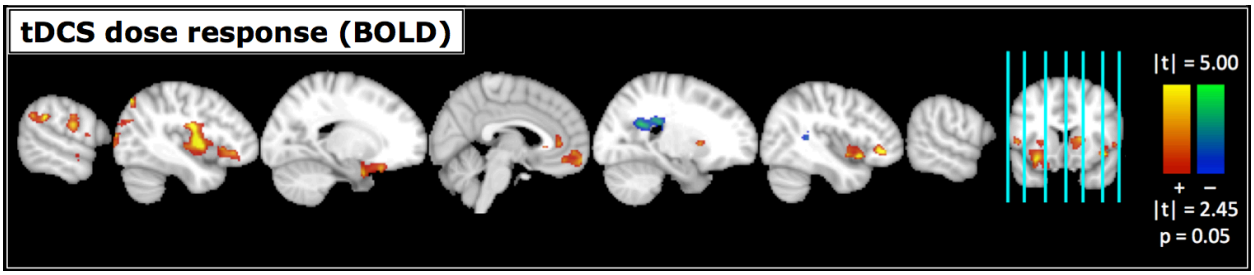

Figure 1. Group level results of the BOLD signal analysis. A significant linear dose response was observed at {L. M1, Insula, ACC, R. Caudate, and L. parietal/occipital lobe}. A significance level of $p < 0.05$, cluster size > 100 was used.

4. Discussion

The second echo of the "#2" implementation was chosen to encode the BOLD contrast in the magnitude signal. The acquired magnitude data was analyzed to identify regions of the brain that respond consistently (across subjects) to tDCS. Among the regions showing a linear dose response to tDCS, L.M1 was site of the cathode electrode, and the rest of the regions have been reported to be functionally interconnected via the insula(92). This finding supports the

hypothesis that tDCS possibly targets brain-networks rather than local regions (reported by Fox et al. (93)). However, it should be noted that these results did not survive correction for multiple comparisons. This could be because the group level analysis is underpowered due to the small number of subjects.

Limitations and Future directions

With the above analysis, we were unable to reliably detect %BOLD changes in individual subjects. This could be due to the linearity assumption implicit in using a GLM. In the case of magnetic fields induced by tDCS, a linear relationship between fields and applied current is reasonable considering the linearity of Ampere's Law and the assumption that current paths do not change across different intensities. However, the linearity assumption may be too strict in the case of the BOLD signal. An alternative could be to use a rank transform approach that would identify regions of the brain responding monotonically to tDCS. Additionally, the drift effects associated with the long stimulation blocks (2 min) may also hinder reliable detection of BOLD changes due to stimulation.

Although BOLD MRI is a popular choice to measure neurophysiological changes, the BOLD signal change is a relative measure, and not individually quantitative. An alternative to BOLD MRI is Arterial Spin Labeling (ASL)(53), which can be used to quantify regional cerebral blood flow (rCBF), a marker for neuronal activity. The ASL sequence quantifies CBF from a ~1% fluctuation in the magnitude signal, and thus is not expected to perturb the SNR of phase or magnitude signals significantly. Additionally, ASL uses the same EPI readout as the "#2" implementation (with a preparatory RF-pulse), and thus can conceivably be integrated into the

existing implementation. Such a technique would enable simultaneous measurements of target engagement (through current induced magnetic fields) and brain-response (through rCBF changes), opening a new avenue for quantitative investigations of tDCS *in vivo*.

5. Conclusion

This chapter demonstrates the feasibility of concurrent measurement of the tDCS current induced magnetic field and the BOLD signal change. This is possible because the BOLD signal is encoded in the 'magnitude' of the MRI signal, while the tDCS current induced magnetic field is encoded exclusively in the 'phase'. A group level analysis of the BOLD data revealed a linear dose response to tDCS in brain regions which have been shown to be functionally connected. However, we were unable to detect reliable BOLD changes in individual subjects. This will be a focus of future research. The capability to reliably visualize tDCS currents (through magnetic fields) as well as the response of the brain (through BOLD fMRI) in individual subjects may open the door to a new field of individualized, precise and noninvasive neuromodulation using tDCS.

Summary and future directions

This dissertation presents the theoretical framework and implementations of a novel MRI technique that enables visualization of the tDCS electric current through quantitative magnetic field mapping. Going forward, we will conduct test-retest experiments to establish reliability of the technique (imaging as well as tDCS). In parallel, we will explore the possibility of improving simulations through measurement-guided tuning of model-parameters. A third direction of research will concentrate on improving the "#2" implementation to enable measurements of tDCS induced neurophysiological changes (BOLD) in individual subjects. In the future, we plan to use the developed technique to evaluate the efficacies of different tDCS montages (including focal HD-tDCS) in a clinical population (depression).

References:

1. Nitsche MA, Cohen LG, Wassermann EM, Priori A, Lang N, Antal A, et al. Transcranial direct current stimulation: State of the art 2008. Brain stimulation. 2008 Jul;1(3):206-23. PubMed PMID: 20633386.

2. Nitsche MA, Paulus W. Excitability changes induced in the human motor cortex by weak transcranial direct current stimulation. The Journal of physiology. 2000 Sep 15;527 Pt 3:633-9. PubMed PMID: 10990547. Pubmed Central PMCID: 2270099.

3. Nitsche MA, Paulus W. Sustained excitability elevations induced by transcranial DC motor cortex stimulation in humans. Neurology. 2001 Nov 27;57(10):1899-901. PubMed PMID: 11723286.

4. Stagg CJ, Nitsche MA. Physiological basis of transcranial direct current stimulation. The Neuroscientist : a review journal bringing neurobiology, neurology and psychiatry. 2011 Feb;17(1):37-53. PubMed PMID: 21343407.

5. Shekhawat GS, Stinear CM, Searchfield GD. Transcranial direct current stimulation intensity and duration effects on tinnitus suppression. Neurorehabilitation and neural repair. 2013 Feb;27(2):164-72. PubMed PMID: 23032310.

6. Murray LM, Edwards DJ, Ruffini G, Labar D, Stampas A, Pascual-Leone A, et al. Intensity dependent effects of transcranial direct current stimulation on corticospinal excitability in chronic spinal cord injury. Archives of physical medicine and rehabilitation. 2015 Apr;96(4 Suppl):S114-21. PubMed PMID: 25461825. Pubmed Central PMCID: 4380548.

7. Woods AJ, Antal A, Bikson M, Boggio PS, Brunoni AR, Celnik P, et al. A technical guide to tDCS, and related non-invasive brain stimulation tools. Clinical neurophysiology : official journal of the International Federation of Clinical Neurophysiology. 2016 Feb;127(2):1031-48. PubMed PMID: 26652115. Pubmed Central PMCID: 4747791.

8. Kuo HI, Bikson M, Datta A, Minhas P, Paulus W, Kuo MF, et al. Comparing cortical plasticity induced by conventional and high-definition 4 x 1 ring tDCS: a neurophysiological study. Brain stimulation. 2013 Jul;6(4):644-8. PubMed PMID: 23149292.

9. Edwards D CM, Datta A, Minhas P, Wassermann EM, Bikson M. Physiological and modeling evidence for focal transcranial electrical brain stimulation in humans: a basis for high-definition tDCS. NeuroImage. 2013.

10. Kidgell DJ, Goodwill AM, Frazer AK, Daly RM. Induction of cortical plasticity and improved motor performance following unilateral and bilateral transcranial direct current stimulation of the primary motor cortex. BMC neuroscience. 2013 Jul 01;14:64. PubMed PMID: 23815634. Pubmed Central PMCID: 3701480.

11. Sehm B, Kipping J, Schafer A, Villringer A, Ragert P. A Comparison between Uni- and Bilateral tDCS Effects on Functional Connectivity of the Human Motor Cortex. Frontiers in human neuroscience. 2013;7:183. PubMed PMID: 23675337. Pubmed Central PMCID: 3646257.

12. Pixa NH, Steinberg F, Doppelmayr M. High-definition transcranial direct current stimulation to both primary motor cortices improves unimanual and bimanual dexterity. Neuroscience letters. 2017 Mar 16;643:84-8. PubMed PMID: 28229937.

13. Cohen Kadosh R, Soskic S, Iuculano T, Kanai R, Walsh V. Modulating neuronal activity produces specific and long-lasting changes in numerical competence. Current biology : CB. 2010 Nov 23;20(22):2016-20. PubMed PMID: 21055945. Pubmed Central PMCID: 2990865.

14. Coffman BA, Clark VP, Parasuraman R. Battery powered thought: enhancement of attention, learning, and memory in healthy adults using transcranial direct current stimulation. NeuroImage. 2014 Jan 15;85 Pt 3:895-908. PubMed PMID: 23933040.

15. Andrade C. Transcranial direct current stimulation for refractory auditory hallucinations in schizophrenia. The Journal of clinical psychiatry. 2013 Nov;74(11):e1054-8. PubMed PMID: 24330906.

16. Brunoni AR, Nitsche MA, Bolognini N, Bikson M, Wagner T, Merabet L, et al. Clinical research with transcranial direct current stimulation (tDCS): challenges and future directions. Brain stimulation. 2012 Jul;5(3):175-95. PubMed PMID: 22037126. Pubmed Central PMCID: 3270156.

17. Hill AT, Rogasch NC, Fitzgerald PB, Hoy KE. Effects of prefrontal bipolar and high-definition transcranial direct current stimulation on cortical reactivity and working memory in healthy adults. NeuroImage. 2017 May 15;152:142-57. PubMed PMID: 28274831.

18. Murphy DN, Boggio P, Fregni F. Transcranial direct current stimulation as a therapeutic tool for the treatment of major depression: insights from past and recent clinical studies. Current opinion in psychiatry. 2009 May;22(3):306-11. PubMed PMID: 19339889.

19. Talsma LJ, Kroese HA, Slagter HA. Boosting Cognition: Effects of Multiple-Session Transcranial Direct Current Stimulation on Working Memory. Journal of cognitive neuroscience. 2017 Apr;29(4):755-68. PubMed PMID: 27897670.

20. Ciechanski P, Kirton A. Transcranial Direct-Current Stimulation Can Enhance Motor Learning in Children. Cerebral cortex. 2017 May 01;27(5):2758-67. PubMed PMID: 27166171.

21. Muszkat D, Polanczyk GV, Dias TG, Brunoni AR. Transcranial Direct Current Stimulation in Child and Adolescent Psychiatry. Journal of child and adolescent psychopharmacology. 2016 Sep;26(7):590-7. PubMed PMID: 27027666.

22. Palm U, Segmiller FM, Epple AN, Freisleder FJ, Koutsouleris N, Schulte-Korne G, et al. Transcranial direct current stimulation in children and adolescents: a comprehensive review. Journal of neural transmission. 2016 Oct;123(10):1219-34. PubMed PMID: 27173384.

23. Bikson M, Grossman P, Thomas C, Zannou AL, Jiang J, Adnan T, et al. Safety of Transcranial Direct Current Stimulation: Evidence Based Update 2016. Brain stimulation. 2016 Sep-Oct;9(5):641-61. PubMed PMID: 27372845. Pubmed Central PMCID: 5007190.

24. Gomez Palacio Schjetnan A, Faraji J, Metz GA, Tatsuno M, Luczak A. Transcranial direct current stimulation in stroke rehabilitation: a review of recent advancements. Stroke research and treatment. 2013;2013:170256. PubMed PMID: 23533955. Pubmed Central PMCID: 3600193.

25. Ahn H, Woods AJ, Kunik ME, Bhattacharjee A, Chen Z, Choi E, et al. Efficacy of transcranial direct current stimulation over primary motor cortex (anode) and contralateral supraorbital area (cathode) on clinical pain severity and mobility performance in persons with knee osteoarthritis: An experimenter- and participant-blinded, randomized, sham-controlled pilot clinical study. Brain stimulation. 2017 May 19. PubMed PMID: 28566193.

26. Assenza G, Campana C, Assenza F, Pellegrino G, Di Pino G, Fabrizio E, et al. Cathodal transcranial direct current stimulation reduces seizure frequency in adults with drug-resistant temporal lobe epilepsy: A sham controlled study. Brain stimulation. 2017 Mar - Apr;10(2):333-5. PubMed PMID: 28017320.

27. Batista EK, Klauss J, Fregni F, Nitsche MA, Nakamura-Palacios EM. A Randomized Placebo-Controlled Trial of Targeted Prefrontal Cortex Modulation with Bilateral tDCS in Patients with Crack-Cocaine Dependence. The international journal of neuropsychopharmacology. 2015 Jun 10;18(12). PubMed PMID: 26065432. Pubmed Central PMCID: 4675977.

28. D'Urso G, Dell'Osso B, Rossi R, Brunoni AR, Bortolomasi M, Ferrucci R, et al. Clinical predictors of acute response to transcranial direct current stimulation (tDCS) in major depression. Journal of affective disorders. 2017 Sep;219:25-30. PubMed PMID: 28505499.

29. Donde C, Amad A, Nieto I, Brunoni AR, Neufeld NH, Bellivier F, et al. Transcranial direct-current stimulation (tDCS) for bipolar depression: A systematic review and meta-analysis. Progress in neuro-psychopharmacology & biological psychiatry. 2017 Aug 01;78:123-31. PubMed PMID: 28552295.

30. Fernandez-Lago H, Bello O, Mora-Cerda F, Montero-Camara J, Fernandez-Del-Olmo MA. Treadmill Walking Combined With Anodal Transcranial Direct Current Stimulation in Parkinson Disease: A Pilot Study of Kinematic and Neurophysiological Effects. American journal of physical medicine & rehabilitation. 2017 Apr 08. PubMed PMID: 28398968.

31. Harvey MP, Lorrain D, Martel M, Bergeron-Vezina K, Houde F, Seguin M, et al. Can we improve pain and sleep in elderly individuals with transcranial direct current stimulation? - Results from a randomized controlled pilot study. Clinical interventions in aging. 2017;12:937-47. PubMed PMID: 28652716. Pubmed Central PMCID: 5472413.

32. Karvigh SA, Motamedi M, Arzani M, Roshan JH. HD-tDCS in refractory lateral frontal lobe epilepsy patients. Seizure. 2017 Apr;47:74-80. PubMed PMID: 28324765.

33. Khedr EM, Omran EAH, Ismail NM, El-Hammady DH, Goma SH, Kotb H, et al. Effects of transcranial direct current stimulation on pain, mood and serum endorphin level in the treatment of fibromyalgia: A double blinded, randomized clinical trial. Brain stimulation. 2017 Jun 23. PubMed PMID: 28684258.

34. Koh CL, Lin JH, Jeng JS, Huang SL, Hsieh CL. Effects of Transcranial direct current stimulation with sensory modulation on stroke motor rehabilitation: A randomized controlled trial. Archives of physical medicine and rehabilitation. 2017 Jun 23. PubMed PMID: 28652065.

35. Kroczek AM, Haussinger FB, Rohe T, Schneider S, Plewnia C, Batra A, et al. Effects of transcranial direct current stimulation on craving, heart-rate variability and prefrontal hemodynamics during smoking cue exposure. Drug and alcohol dependence. 2016 Nov 01;168:123-7. PubMed PMID: 27639130.

36. Lindenberg R, Renga V, Zhu LL, Nair D, Schlaug G. Bihemispheric brain stimulation facilitates motor recovery in chronic stroke patients. Neurology. 2010 Dec 14;75(24):2176-84. PubMed PMID: 21068427. Pubmed Central PMCID: 3013585.

37. Schlaug G, Renga V, Nair D. Transcranial direct current stimulation in stroke recovery. Archives of neurology. 2008 Dec;65(12):1571-6. PubMed PMID: 19064743. Pubmed Central PMCID: 2779259.

38. Witt K, Kalbe E, Erasmi R, Ebersbach G. [Nonpharmacological treatment procedures for Parkinson's disease]. Der Nervenarzt. 2017 Apr;88(4):383-90. PubMed PMID: 28251243. Nichtmedikamentose Therapieverfahren beim Morbus Parkinson.

39. Yotnuengnit P, Bhidayasiri R, Donkhan R, Chaluaysrimuang J, Piravej K. Effects of Transcranial Direct Current Stimulation Plus Physical Therapy on Gait in Patients With Parkinson Disease: A Randomized Controlled Trial. American journal of physical medicine & rehabilitation. 2017 Jun 24. PubMed PMID: 28650857.

40. Shin YI, Foerster A, Nitsche MA. Transcranial direct current stimulation (tDCS) - application in neuropsychology. Neuropsychologia. 2015 Mar;69:154-75. PubMed PMID: 25656568.

41. Poreisz C, Boros K, Antal A, Paulus W. Safety aspects of transcranial direct current stimulation concerning healthy subjects and patients. Brain research bulletin. 2007 May 30;72(4-6):208-14. PubMed PMID: 17452283.

42. Miranda PC, Lomarev M, Hallett M. Modeling the current distribution during transcranial direct current stimulation. Clinical neurophysiology : official journal of the International Federation of Clinical Neurophysiology. 2006 Jul;117(7):1623-9. PubMed PMID: 16762592.

43. Rush S, Driscoll D. Current distribution in the brain from surface electrodes. Anesth Analg. 1968;47(6).

44. Bikson M, Rahman A, Datta A. Computational models of transcranial direct current stimulation. Clinical EEG and neuroscience. 2012 Jul;43(3):176-83. PubMed PMID: 22956646.

45. Truong DQ, Adair D, Bikson M. Computer-Based Models of tDCS and tACS. 2016.

46. Truong DQ, Magerowski G, Blackburn GL, Bikson M, Alonso-Alonso M. Computational modeling of transcranial direct current stimulation (tDCS) in obesity: Impact of head fat and dose guidelines. NeuroImage Clinical. 2013;2:759-66. PubMed PMID: 24159560. Pubmed Central PMCID: 3778260.

47. Kessler SK, Minhas P, Woods AJ, Rosen A, Gorman C, Bikson M. Dosage considerations for transcranial direct current stimulation in children: a computational modeling study. PloS one. 2013;8(9):e76112. PubMed PMID: 24086698. Pubmed Central PMCID: 3785412.

48. Datta A, Bansal V, Diaz J, Patel J, Reato D, Bikson M. Gyri-precise head model of transcranial direct current stimulation: improved spatial focality using a ring electrode versus conventional rectangular pad. Brain stimulation. 2009 Oct;2(4):201-7, 7 e1. PubMed PMID: 20648973. Pubmed Central PMCID: 2790295.

49. Roche N, Geiger M, Bussel B. Mechanisms underlying transcranial direct current stimulation in rehabilitation. Annals of physical and rehabilitation medicine. 2015 Sep;58(4):214-9. PubMed PMID: 26189791.

50. Buxton RB. The physics of functional magnetic resonance imaging (fMRI). Reports on progress in physics Physical Society. 2013 Sep;76(9):096601. PubMed PMID: 24006360. Pubmed Central PMCID: 4376284.

51. Kwong KK, Belliveau JW, Chesler DA, Goldberg IE, Weisskoff RM, Poncelet BP, et al. Dynamic magnetic resonance imaging of human brain activity during primary sensory stimulation. Proceedings of the National Academy of Sciences of the United States of America. 1992 Jun 15;89(12):5675-9. PubMed PMID: 1608978. Pubmed Central PMCID: 49355.

52. Ogawa S, Lee TM, Kay AR, Tank DW. Brain magnetic resonance imaging with contrast dependent on blood oxygenation. Proceedings of the National Academy of Sciences of the United States of America. 1990 Dec;87(24):9868-72. PubMed PMID: 2124706. Pubmed Central PMCID: 55275.

53. Detre JA, Rao H, Wang DJ, Chen YF, Wang Z. Applications of arterial spin labeled MRI in the brain. Journal of magnetic resonance imaging : JMRI. 2012 May;35(5):1026-37. PubMed PMID: 22246782. Pubmed Central PMCID: 3326188.

54. Antal A, Polania R, Schmidt-Samoa C, Dechent P, Paulus W. Transcranial direct current stimulation over the primary motor cortex during fMRI. NeuroImage. 2011 Mar 15;55(2):590-6. PubMed PMID: 21211569.

55. Kwon YH, Jang SH. The enhanced cortical activation induced by transcranial direct current stimulation during hand movements. Neuroscience letters. 2011 Apr 01;492(2):105-8. PubMed PMID: 21291959.

56. Polania R, Paulus W, Antal A, Nitsche MA. Introducing graph theory to track for neuroplastic alterations in the resting human brain: a transcranial direct current stimulation study. NeuroImage. 2011 Feb 01;54(3):2287-96. PubMed PMID: 20932916.

57. Polania R, Paulus W, Nitsche MA. Modulating cortico-striatal and thalamo-cortical functional connectivity with transcranial direct current stimulation. Human brain mapping. 2012 Oct;33(10):2499-508. PubMed PMID: 21922602.

58. Saiote C, Turi Z, Paulus W, Antal A. Combining functional magnetic resonance imaging with transcranial electrical stimulation. Frontiers in human neuroscience. 2013;7:435. PubMed PMID: 23935578. Pubmed Central PMCID: 3733022.

59. Clark VP, Coffman BA, Mayer AR, Weisend MP, Lane TD, Calhoun VD, et al. TDCS guided using fMRI significantly accelerates learning to identify concealed objects. NeuroImage. 2012 Jan 02;59(1):117-28. PubMed PMID: 21094258. Pubmed Central PMCID: 3387543.

60. Zheng X, Alsop DC, Schlaug G. Effects of transcranial direct current stimulation (tDCS) on human regional cerebral blood flow. NeuroImage. 2011 Sep 01;58(1):26-33. PubMed PMID: 21703350. Pubmed Central PMCID: 3155947.

61. Joy ML, Scott G, Henkelman M. In vivo detection of applied electric currents by magnetic resonance imaging. Magnetic resonance in medicine. 1989;7(1).

62. Joy ML. MR current density and conductivity imaging: the state of the art. Conference proceedings : Annual International Conference of the IEEE Engineering in Medicine and Biology Society IEEE Engineering in Medicine and Biology Society Annual Conference. 2004;7:5315-9. PubMed PMID: 17271541.

63. Wang D, DeMonte TP, Ma W, Joy ML, Nachman AI. Multislice radio-frequency current density imaging. IEEE transactions on medical imaging. 2009 Jul;28(7):1083-92. PubMed PMID: 19150780.

64. Wang D, Ma W, Demonte TP, Nachman AI, Joy ML. Radio-frequency current density imaging based on a 180 (degrees) sample rotation with feasibility study of full current density vector reconstruction. IEEE transactions on medical imaging. 2011 Feb;30(2):327-37. PubMed PMID: 20875968.

65. Scott G, Joy ML, Armstrong RL, Henkelman RM. Rotating frame RF current density imaging. Magnetic resonance in medicine.33(3).

66. Chauhan M, Vidya Shankar R, Ashok Kumar N, Kodibagkar VD, Sadleir R. Multishot echo-planar MREIT for fast imaging of conductivity, current density, and electric field distributions. Magnetic resonance in medicine. 2017 Feb 16. PubMed PMID: 28205251.

67. Kasinadhuni AK, Indahlastari A, Chauhan M, Schar M, Mareci TH, Sadleir RJ. Imaging of current flow in the human head during transcranial electrical therapy. Brain stimulation. 2017 Jul - Aug;10(4):764-72. PubMed PMID: 28457836. Pubmed Central PMCID: 5513732.

68. Seo JK, Woo EJ. Electrical tissue property imaging at low frequency using MREIT. IEEE transactions on bio-medical engineering. 2014 May;61(5):1390-9. PubMed PMID: 24759274.

69. Schenck JF. The role of magnetic susceptibility in magnetic resonance imaging: MRI magnetic compatibility of the first and second kinds. Medical physics. 1996 Jun;23(6):815-50. PubMed PMID: 8798169.

70. Jog MV, Smith RX, Jann K, Dunn W, Lafon B, Truong D, et al. In-vivo Imaging of Magnetic Fields Induced by Transcranial Direct Current Stimulation (tDCS) in Human Brain using MRI. Scientific reports. 2016 Oct 04;6:34385. PubMed PMID: 27698358. Pubmed Central PMCID: 5048181

71. Kim DH, Chauhan M, Kim MO, Jeong WC, Kim HJ, Sersa I, et al. Frequency-dependent conductivity contrast for tissue characterization using a dual-frequency range conductivity mapping magnetic resonance method. IEEE transactions on medical imaging. 2015 Feb;34(2):507-13. PubMed PMID: 25312916.

72. Chai Y, Bi G, Wang L, Xu F, Wu R, Zhou X, et al. Direct detection of optogenetically evoked oscillatory neuronal electrical activity in rats using SLOE sequence. NeuroImage. 2016 Jan 15;125:533-43. PubMed PMID: 26518631.

73. Gudbjartsson H, Patz S. The Rician distribution of noisy MRI data. Magnetic resonance in medicine. 1995 Dec;34(6):910-4. PubMed PMID: 8598820. Pubmed Central PMCID: 2254141.

74. Barnhill E, Kennedy P, Hammer S, van Beek EJ, Brown C, Roberts N. Statistical mapping of the effect of knee extension on thigh muscle viscoelastic properties using magnetic resonance elastography. Physiological measurement. 2013 Dec;34(12):1675-98. PubMed PMID: 24254405.

75. Schindelin J, Arganda-Carreras I, Frise E, Kaynig V, Longair M, Pietzsch T, et al. Fiji: an open-source platform for biological-image analysis. Nature methods. 2012 Jun 28;9(7):676-82. PubMed PMID: 22743772. Pubmed Central PMCID: 3855844.

76. Forman S, Cohen J, Fitzgerald M, Eddy W, Mintun M, Noll D. Improved assessment of significant activation in functional magnetic resonance imaging (fMRI): use of a cluster-size threshold. Magnetic resonance in medicine. 1995;33(5).

77. Vitali P, Avanzini G, Caposio L, Fallica E, Grigoletti L, Maccagnano E, et al. Cortical location of 10–20 system electrodes on normalized cortical MRI surfaces. International Journal of Bioelectromagnetism. 2002;4(2).

78. Quéval L. BSmag Toolbox User Manual. Tech report, Dept Elect Eng, University of Applied Sciences Dusseldorf, Germany Available: http://wwwlquevalcom 2015.

79. Wagner T, Zahn M, Grodzinsky A, Pascual-Leone A. Three-dimensional head model simulation of transcranial magnetic stimulation. IEEE Trans Biomed Eng. 2004;51(9).

80. Gabriel C, Gabriel S, Corthout E. The dielectric properties of biological tissues: I. Literature survey. Phys Med Biol. 1996;41(11).

81. Antal A, Bikson M, Datta A, Lafon B, Dechent P, Parra LC, et al. Imaging artifacts induced by electrical stimulation during conventional fMRI of the brain. NeuroImage. 2014 Jan 15;85 Pt 3:1040-7. PubMed PMID: 23099102. Pubmed Central PMCID: 3759658.

82. Garcia-Cossio E, Witkowski M, Robinson SE, Cohen LG, Birbaumer N, Soekadar SR. Simultaneous transcranial direct current stimulation (tDCS) and whole-head magnetoencephalography (MEG): assessing the impact of tDCS on slow cortical magnetic fields. NeuroImage. 2016 Oct 15;140:33-40. PubMed PMID: 26455796. Pubmed Central PMCID: 5108059.

83. Hanley CJ, Singh KD, McGonigle DJ. Transcranial modulation of brain oscillatory responses: A concurrent tDCS-MEG investigation. NeuroImage. 2016 Oct 15;140:20-32. PubMed PMID: 26706447.

84. Mancini M, Brignani D, Conforto S, Mauri P, Miniussi C, Pellicciari MC. Assessing cortical synchronization during transcranial direct current stimulation: A graph-theoretical analysis. NeuroImage. 2016 Oct 15;140:57-65. PubMed PMID: 27268424.

85. Faria P, Hallett M, Miranda PC. A finite element analysis of the effect of electrode area and inter-electrode distance on the spatial distribution of the current density in tDCS. Journal of neural engineering. 2011 Dec;8(6):066017. PubMed PMID: 22086257. Pubmed Central PMCID: 3411515.

86. Thielscher A, Antunes A, Saturnino GB. Field modeling for transcranial magnetic stimulation: A useful tool to understand the physiological effects of TMS? Conference proceedings : Annual International Conference of the IEEE Engineering in Medicine and Biology Society IEEE Engineering in Medicine and Biology Society Annual Conference. 2015;2015:222-5. PubMed PMID: 26736240.

87. Windhoff M, Opitz A, Thielscher A. Electric field calculations in brain stimulation based on finite elements: an optimized processing pipeline for the generation and usage of accurate individual head models. Human brain mapping. 2013 Apr;34(4):923-35. PubMed PMID: 22109746.

88. Akhtari M, Mandelkern M, Bui D, Salamon N, Vinters HV, Mathern GW. Variable anisotropic brain electrical conductivities in epileptogenic foci. Brain topography. 2010 Sep;23(3):292-300. PubMed PMID: 20440549. Pubmed Central PMCID: 2914871.

89. Bjorklund S, Ruzgas T, Nowacka A, Dahi I, Topgaard D, Sparr E, et al. Skin membrane electrical impedance properties under the influence of a varying water gradient. Biophysical journal. 2013 Jun 18;104(12):2639-50. PubMed PMID: 23790372. Pubmed Central PMCID: 3686338.

90. Kruger G, Glover GH. Physiological noise in oxygenation-sensitive magnetic resonance imaging. Magnetic resonance in medicine. 2001 Oct;46(4):631-7. PubMed PMID: 11590638.

91. Jog MA, Yan L, Kilroy E, Krasileva K, Jann K, LeClair H, et al. Developmental trajectories of cerebral blood flow and oxidative metabolism at baseline and during working memory tasks. NeuroImage. 2016 Jul 01;134:587-96. PubMed PMID: 27103136.

92. Cauda F, D'Agata F, Sacco K, Duca S, Geminiani G, Vercelli A. Functional connectivity of the insula in the resting brain. NeuroImage. 2011 Mar 01;55(1):8-23. PubMed PMID: 21111053.

93. Fox MD, Buckner RL, Liu H, Chakravarty MM, Lozano AM, Pascual-Leone A. Resting-state networks link invasive and noninvasive brain stimulation across diverse psychiatric and neurological diseases. Proceedings of the National Academy of Sciences of the United States of America. 2014 Oct 14;111(41):E4367-75. PubMed PMID: 25267639. Pubmed Central PMCID: 4205651.